The Astrophysical Journal, 997:340 (23pp), 2026 February 1 https://doi.org/10.3847/1538-4357/ae2602


# The ALMA-QUARKS Survey: Hot Molecular Cores Are a Long-standing Phenomenon in the Evolution of Massive Protostars

Dezhao Meng[1,2,3], Tie Liu[2,3], Jarken Esimbek[1,2,4], Sheng-Li Qin[5], Guido Garay[6,7], Paul F. Goldsmith[8], Jianjun Zhou[1,2,4], Xindi Tang[1,2,4], Wenyu Jiao[3], Yan-Kun Zhang[3], Fengwei Xu[9], Siju Zhang[6], Anandmayee Tej[10], Leonardo Bronfman[6], Aiyuan Yang[11], Sami Dib[12], Swagat R. Das[6], Jihye Hwang[13,14], Archana Soam[15], Yisheng Qiu[16], Dalei Li[1,2,4], Yuxin He[1,2,4], Gang Wu[1,2,4], Lokesh Dewangan[17], James O. Chibueze[18,19], Pablo García[7,20], Prasanta Gorai[21,22], Naval Kishor Bhadari[9], Yong Zhang[23], Patricio Sanhueza[24], Yongquan Luo[1,2], Jia-Hang Zou[3,5], Kee-Tae Kim[25,26], Dongting Yang[5], Lei Zhu[7], Xunchuan Liu[3], Macleod Gordon[1], and Yingxiu Ma[1,4]

[1] State Key Laboratory of Radio Astronomy and Technology, Xinjiang Astronomical Observatory, Chinese Academy of Sciences, 150 Science 1-Street, Urumqi, Xinjiang, 830011, People's Republic of China; mengdezhao@xao.ac.cn, jarken@xao.ac.cn
[2] University of Chinese Academy of Sciences, Beijing 100080, People's Republic of China; liutie@shao.ac.cn
[3] State Key Laboratory of Radio Astronomy and Technology, Shanghai Astronomical Observatory, Chinese Academy of Sciences, 80 Nandan Road, Shanghai 200030, People's Republic of China
[4] Xinjiang Key Laboratory of Radio Astrophysics, Urumqi 830011, People's Republic of China
[5] School of Physics and Astronomy, Yunnan University, Kunming 650091, People's Republic of China
[6] Departamento de Astronomía, Universidad de Chile, Las Condes, 7591245 Santiago, Chile
[7] Chinese Academy of Sciences South America Center for Astronomy, National Astronomical Observatories, CAS, Beijing 100101, People's Republic of China
[8] Jet Propulsion Laboratory, California Institute of Technology, 4800 Oak Grove Drive, Pasadena, CA 91109, USA
[9] Kavli Institute for Astronomy and Astrophysics, Peking University, 5 Yiheyuan Road, Haidian District, Beijing 100871, People's Republic of China
[10] Indian Institute of Space Science and Technology, Thiruvananthapuram 695 547, India
[11] National Astronomical Observatories, Chinese Academy of Sciences, A20 Datun Road, Chaoyang District, Beijing, 100101, People's Republic of China
[12] Max Planck Institute for Astronomy, Königstuhl 17, 69117, Heidelberg, Germany
[13] Institute for Advanced Study, Kyushu University, Japan
[14] Department of Earth and Planetary Sciences, Faculty of Science, Kyushu University, Nishi-ku, Fukuoka 819-0395, Japan
[15] Indian Institute of Astrophysics, II Block, Koramangala, Bengaluru 560034, India
[16] Research Center for Astronomical Computing, Zhejiang Laboratory, Hangzhou 311121, People's Republic of China
[17] Physical Research Laboratory, Navrangpura, Ahmedabad 380009, India
[18] Department of Mathematical Sciences, University of South Africa, Cnr Christian de Wet Rd and Pioneer Avenue, Florida Park, 1709, Roodepoort, South Africa
[19] Department of Physics and Astronomy, Faculty of Physical Sciences, University of Nigeria, Carver Building, 1 University Road, Nsukka 410001, Nigeria
[20] Instituto de Astronomía, Universidad Católica del Norte, Av. Angamos 0610, Antofagasta, Chile
[21] Rosseland Centre for Solar Physics, University of Oslo, PO Box 1029 Blindern, 0315 Oslo, Norway
[22] Institute of Theoretical Astrophysics, University of Oslo, PO Box 1029 Blindern, 0315 Oslo, Norway
[23] School of Physics and Astronomy, Sun Yat-sen University, 2 Daxue Road, Tangjia, Zhuhai, Guangdong Province, People's Republic of China
[24] Department of Astronomy, School of Science, The University of Tokyo, 7-3-1 Hongo, Bunkyo-ku, Tokyo 113-0033, Japan
[25] Korea Astronomy and Space Science Institute, 776 Daedeokdaero, Yuseong-gu, Daejeon 34055, Republic of Korea
[26] University of Science and Technology, Korea (UST), 217 Gajeong-ro, Yuseong-gu, Daejeon 34113, Republic of Korea
*Received 2025 July 24; revised 2025 November 25; accepted 2025 November 29; published 2026 January 30*

## Abstract

We present an analysis of the QUARKS survey sample, focusing on protoclusters where hot molecular cores (HMCs; traced by $CH_3CN$ (12–11)) and HC/UC H II regions (traced by H30$\alpha$/H40$\alpha$) coexist. Using the high-resolution, high-sensitivity 1.3 mm data from the QUARKS survey, we identify 125 hot molecular fragments (HMFs), which represent the substructures of HMCs at higher resolution. From line integrated intensity maps of $CH_3CN$ ($12_3$–$11_3$) and H30$\alpha$, we resolve the spatial distribution of HMFs and HC/UC H II regions. By combining with observations of $^{12}CO$ (2–1) outflows and 1.3 mm continuum, we classify HMFs into four types: HMFs associated with jetlike outflow, wide-angle outflow, and nondetectable outflow and shell-like HMFs near HC/UC H II regions. This diversity possibly indicates that the hot core could be a polymorphic and long-standing phenomenon in the evolution of massive protostars. The separation between HMFs and H30$\alpha$/H40$\alpha$ emission suggests that sequential high-mass star formation within young protoclusters is not likely related to feedback mechanisms.

*Unified Astronomy Thesaurus concepts:* Star formation (1569); Protostars (1302); Star forming regions (1565)

## 1. Introduction

High-mass stars ($M_\star \gtrsim 8\ M_\odot$) play a crucial role in galactic evolution by shaping galactic structures and serving as primary sources of heavy elements and ultraviolet (UV) radiation in the interstellar medium (ISM; H. Zinnecker & H. W. Yorke 2007). However, the formation and evolution of high-mass stars remain poorly understood. Newly formed high-mass protostars heat their surrounding material with temperatures exceeding 100 K, forming hot cores—compact, dense regions ($\lesssim$0.1 pc, $n_{H_2} \gtrsim 10^6\ cm^{-3}$; e.g., G. Garay & S. Lizano 1999; M. Osorio et al. 1999; S. Kurtz et al. 2000; R. Cesaroni 2005; S.-L. Qin et al. 2022; Z.-Y. Li et al. 2025), rich in complex organic molecules (COMs; molecules containing carbon and

consisting of six or more atoms). These hot cores are thought to represent an early evolutionary stage of high-mass star formation, being precursors to evolved H II regions (e.g., C. R. Purcell 2006; H. Beuther et al. 2007; T. Gerner et al. 2014, 2015; R. Choudhury et al. 2015; R. Miyawaki et al. 2021). Hot cores provide critical insights into high-mass star formation, as the detected COMs serve as excellent tracers of both the physical conditions and chemical processes occurring in the immediate environments of high-mass protostars (M. T. Beltrán et al. 2018; J. K. Jørgensen et al. 2020; C. Gieser et al. 2021; G. M. Williams et al. 2022; K. Taniguchi et al. 2023; I. Jimenez-Serra et al. 2025; T. Sakai et al. 2025).

Extensive studies of hot cores have been carried out with single-dish radio telescopes but are limited by poor angular resolution (P. Schilke et al. 1997, 2001, 2006; E. Gibb et al. 2000; F. F. S. van der Tak et al. 2000; S. E. Bisschop et al. 2007; F. Fontani et al. 2007; A. Belloche et al. 2013; D. T. Halfen et al. 2013; N. R. Crockett et al. 2014; J. L. Neill et al. 2014; T. Möller et al. 2021; S. Nickerson et al. 2021). Recent advances in millimeter/submillimeter interferometric arrays (e.g., the Submillimeter Array, SMA, NOEMA, and the Atacama Large Millimeter/submillimeter Array, ALMA), with their superior spatial resolution and sensitivity, have enabled detailed investigations of the physical and chemical properties of hot cores. However, most interferometric studies of hot cores have focused on either individual sources or small samples (S.-Y. Liu et al. 2001, 2002; S.-L. Qin et al. 2008, 2010, 2015; H. Beuther et al. 2009; Y. Wu et al. 2014; E. G. Bøgelund et al. 2019; J. C. Mottram et al. 2020; A. Fuente et al. 2021; C. Gieser et al. 2021; C. J. Law et al. 2021; S. J. van der Walt et al. 2021; F.-W. Xu et al. 2023; F. Xu et al. 2024a). The ALMA Three-millimeter Observations of Massive Star-forming regions (ATOMS; Project ID: 2019.1.00685.S; PI: Tie Liu) survey (T. Liu et al. 2020) recently targeted 146 active high-mass star-forming regions at moderately high angular resolution ($\sim 2''$). Based on the ATOMS survey, S.-L. Qin et al. (2022) identified 60 hot cores by using $C_2H_5CN$, $CH_3OCHO$, and $CH_3OH$ lines. Notably, in 24 of these hot cores, the COM emission distributions were spatially offset from the 3 mm continuum emission, particularly where the 3 mm continuum emission contains contributions from both dust and free–free emission associated with hypercompact/ultracompact H II (HC/UC H II) regions. Nevertheless, the limited resolution of ATOMS prevents definitive discrimination between two possible scenarios for the COMs emission near HC/UC H II regions: (1) residual molecular gas adjacent to the ionized region versus (2) a separate source at a different evolutionary stage (I. Jimenez-Serra et al. 2025). In the latter case, an important question arises as to whether the hot cores around these HC/UC H II regions could have been triggered by HC/UC H II feedback. Radiation pressure and stellar winds from massive stars can compress the ISM and trigger subsequent star formation in dense layers. This so-called "collect-and-collapse" process has been revealed at the borders of several HC/UC H II regions over the past decades (L. Deharveng et al. 2003, 2005, 2008; A. Zavagno et al. 2006, 2007; M. Pomarès et al. 2009; A. Petriella et al. 2010; J. Brand et al. 2011; T. Liu et al. 2012, 2017; H.-L. Liu et al. 2015, 2016; J. Zhou et al. 2020). A high-resolution, statistically significant survey of hot cores around HC/UC H II regions is therefore crucial for exploring the sequential star formation within young protoclusters.

The Querying Underlying mechanisms of massive star formation with ALMA-Resolved gas Kinematics and Structures (QUARKS; Project ID: 2021.1.00095.S; PIs: Lei Zhu, Guido Garay, and Tie Liu) survey (X. Liu et al. 2024; F. Xu et al. 2024b; D. Yang et al. 2025) has observed 139 protoclusters (selected from the ATOMS sample) at 1.3 mm, achieving higher angular resolution and more comprehensive molecular line coverage than the ATOMS survey. Thus, we utilize the QUARKS data to resolve the spatial distribution of COMs in the vicinity of HC/UC H II regions, thereby providing new insights into the hot molecular core (HMC) phase of high-mass star formation and offering implications for stellar feedback within young protoclusters.

## 2. The Sample and Observations

The QUARKS survey observed 139 massive protoclusters in ALMA Band 6. For each source, observations were conducted using the Atacama Compact 7 m Array (ACA) and the ALMA 12 m array in C-2 (TM2) and C-5 (TM1) configurations. The combined data from these three configurations provide a resolution of $\sim 0.''3$, an rms noise ($\sigma$) in a wide range from 0.1 to several mJy beam$^{-1}$ for 1.3 mm continuum emission, and a maximum recoverable scale of $\sim 27''$. The typical noise level for the lines is $\sim$3 mJy beam$^{-1}$ per 0.976 MHz channel ($\sim$1.3 km s$^{-1}$). More detailed information on observation and data reduction can be found in X. Liu et al. (2024), F. Xu et al. (2024b), and D. Yang et al. (2025). In this work, we use the 1.3 mm continuum emission data, as well as line emission data of $CH_3CN$ (12–11), H30$\alpha$ (for fields lacking H30$\alpha$ detections, we substitute ATOMS Band 3 H40$\alpha$), and $^{12}$CO (2–1).

From the ATOMS survey, we first selected fields exhibiting H40$\alpha$ emissions from H40$\alpha$ line integrated intensity maps (above 5$\sigma$). This initial selection ensured that all targets host ionized gas associated with HC/UC H II regions. Subsequently, by combining QUARKS $CH_3CN$ (12–11) channel maps and spectra, we further narrowed down the selection to fields showing $CH_3CN$ (12–11) emissions (above 5$\sigma$) from the initially chosen sample. Through this two-step selection, our sample contains 43 fields, 10 of which lacked H30$\alpha$ detections in QUARKS Band 6 but were detected in H40$\alpha$ at Band 3. Table A1 lists the basic parameters of this sample, including source IDs in our sample (column (1)), IRAS names (column (2)), coordinates (columns (3) and (4)), systemic velocities ($V_{\rm LSR}$; column (5)), distances from the Sun (column (6)), galactocentric distances ($R_{\rm GC}$; column (7)), effective radius (column (8)), dust temperature ($T_{\rm dust}$; column (9)), bolometric luminosity ($L_{\rm bol}$; column (10)), and clump masses ($M_{\rm clump}$; column (11)). Columns (2)–(6) are from X. Liu et al. (2024), while columns (7)–(11) are from T. Liu et al. (2020). In this sample, different evolutionary stages of high-mass star formation coexist within protoclusters, including hot cores and HC/UC H II regions. The HC/UC H II regions are identified via hydrogen radio recombination lines (H30$\alpha$ or H40$\alpha$), while the hot cores are traced using $CH_3CN$ (12–11) emission.

For the analysis, we primarily used H30$\alpha$ where available, given its higher angular resolution in Band 6. In the few cases where H30$\alpha$ data were not available, H40$\alpha$ was used instead to trace the ionized gas.

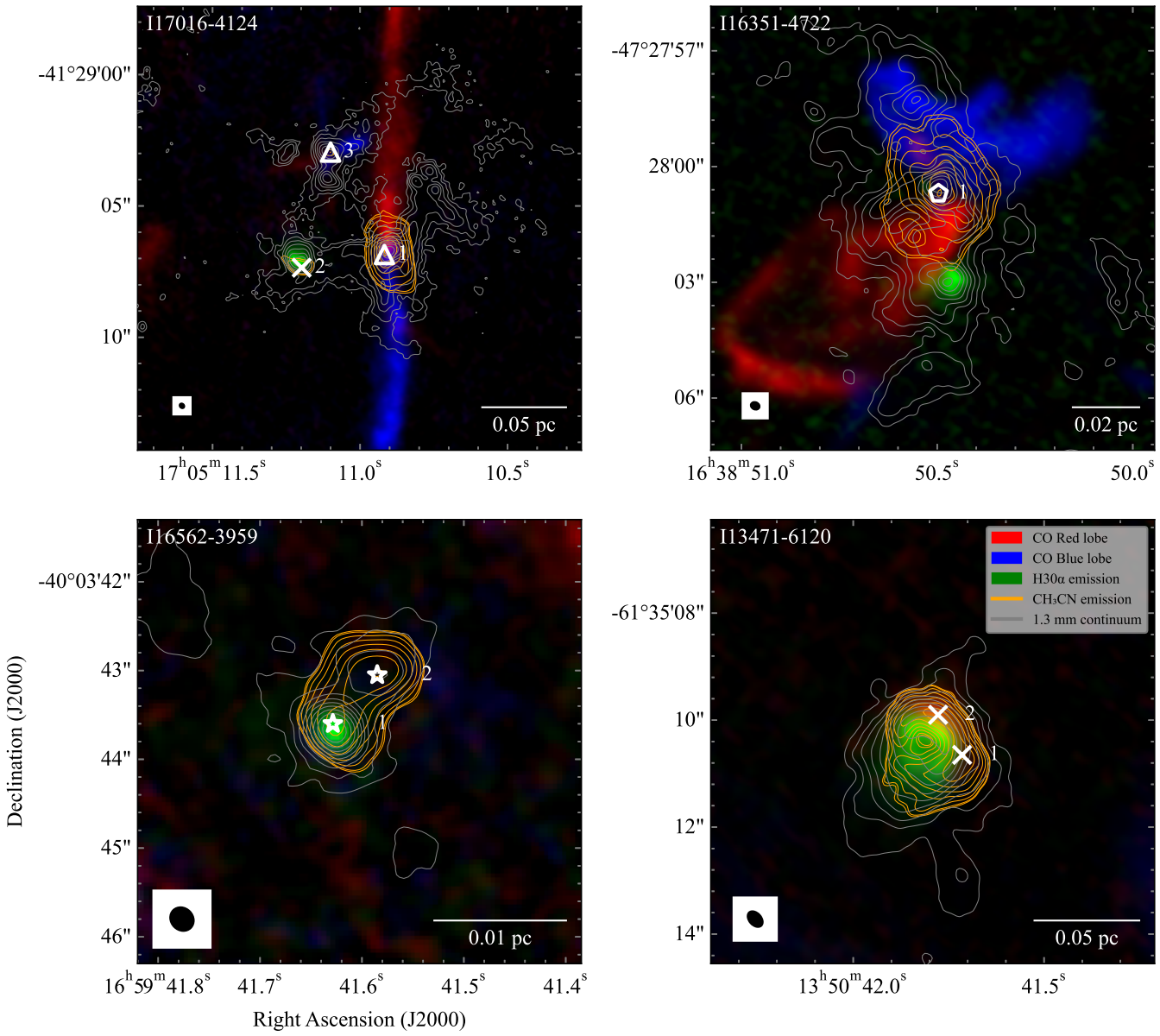


**Figure 1.** Images of the hydrogen recombination line emission and the outflow for four exemplar sources. The background shows the three-color image composed by the redshifted $^{12}$CO (2–1) (red), H30$\alpha$ integrated line emission (green), and blueshifted $^{12}$CO (2–1) (blue). The gray and orange contours represent the 1.3 mm continuum and the $CH_3CN$ ($12_3$–$11_3$) integrated line emission, respectively. The H30$\alpha$ integrated velocity range is [Vlsr–40 km s$^{-1}$, Vlsr+40 km s$^{-1}$], where Vlsr is the central velocity (Table C1, column (9)). For $CH_3CN$ ($12_3$–$11_3$), the integrated velocity ranges are different for different fields. The contour levels were plotted from 3$\sigma$ to the peak intensity of the field, with eight logarithmically spaced contours between these values. White markers mark the positions of different type of HMFs: triangles (jetlike outflow), pentagon (wide-angle outflow), stars (no/weak outflow), and crosses (shell-like shape). The synthesized beams are shown in the lower left corner, and the scale bar is indicated in the lower right corner of each image.

## 3. Results

Figure 1 presents four examples of sources present in the sample. The HC/UC H II region candidates, traced by H30$\alpha$, show different evolutionary stages, from compact early phases to expanding cometary structures. $^{12}$CO (2–1) reveals the outflows driven by young stellar objects (YSOs). The hot core candidates, indicated by $CH_3CN$ ($12_3$–$11_3$) emission, exhibit diverse characteristics, with some driving bipolar outflows (e.g., I17016-4124) while others show only weak or non-detectable outflows (e.g., I16562-3959). Zoom-in views of the images for all selected sources are presented in Figure D1.

### 3.1. Identification of Hot Molecular Fragments

HMCs do not have a clear definition in the literature, but they are usually referred to as gas structures with size $\lesssim$0.1 pc, number density $n_{H_2} \gtrsim 10^6\,cm^{-3}$, and gas temperature $T > 100$ K and are rich in COMs (G. Garay & S. Lizano 1999; M. Osorio et al. 1999; S. Kurtz et al. 2000; R. Cesaroni 2005; S.-L. Qin et al. 2022; Z.-Y. Li et al. 2025). We use the ACA or ACA+TM2 data ($\sim$1″, or 0.023 pc at the median distance of our sample, 4.76 kpc) to identify HMCs, following the similar procedure in S.-L. Qin et al. (2022). These cores correspond to what earlier, lower-resolution studies referred to

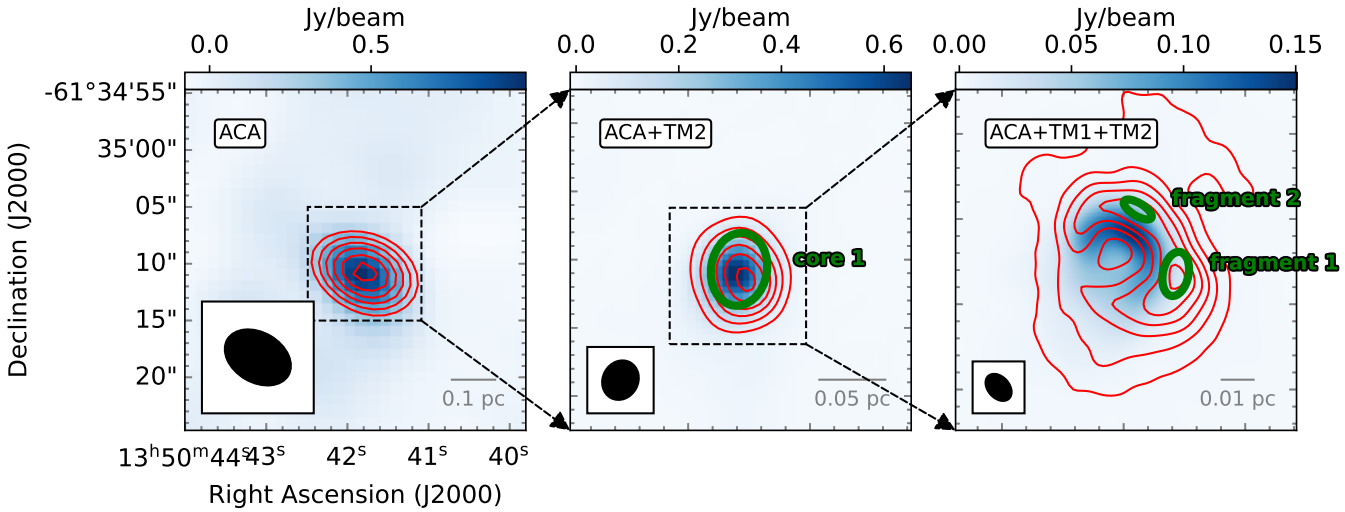


**Figure 2.** Example of `astrodendro` results at different scales. The left, middle, and right panels show data from ACA (F. Xu et al. 2024b), ACA+TM2 (D. Yang et al. 2025), and ACA+TM1+TM2 (X. Liu et al. 2024), respectively. The background shows the 1.3 mm continuum. The red contours represent the integrated intensity of $CH_3CN$ (12–11), with contour levels ranging from $3\sigma$ to $0.95\times$ the peak value, evenly spaced into five levels. The green ellipses outline the structures identified by `astrodendro`. The synthesized beams (left panel: $\sim5''$; middle panel: $\sim1''$; right panel: $\sim0.3''$) are shown in the lower left corner, and the scale bar is indicated in the lower right corner of each panel.

as hot cores, which likely imply the presence of one or several embedded objects.

In addition, we use the ACA+TM1+TM2 data ($\sim0.''3$, or 0.006 pc at 4.76 kpc) to identify the internal substructures within HMCs: hot molecular fragments (HMFs). It is important to note that our use of the term "HMF" does not necessarily imply the presence of an embedded object; rather, it refers to hot emission structures of molecular gas regardless of whether they are internally or externally illuminated objects (G. Garay & S. Lizano 1999). Therefore, two terms are used in this paper to describe hot molecular structures: HMCs in lower-resolution data and HMFs in higher-resolution data. It should be noted that HMCs and HMFs refer to the same physical entities, observed at different spatial resolutions. Figure 2 presents an example at different resolutions. The left and middle panels show the HMC identified at lower resolution, while the right panel reveals that this HMC fragments into two HMFs at higher resolution. In the discussion section, we mainly use HMFs for analysis. In the following, we describe the details of identifying HMCs and HMFs.

The main characteristic of an HMC is its chemical richness, exhibiting emission from numerous COMs. Many studies utilize different COMs to identify HMCs. For example, M. Bonfand et al. (2024) established a comprehensive census of HMC candidates based on the detection of two $CH_3OCHO$ emission lines. In this work, we use $CH_3CN$ (12–11) to trace and identify HMFs and HMCs. $CH_3CN$ (12–11) has been demonstrated to be a good tracer of HMCs by V. Rosero et al. (2013). HMFs were extracted from the $CH_3CN$ ($12_3$–$11_3$) integrated intensity maps in the ACA+TM1+TM2 combined data using the `astrodendro` package.[27] `astrodendro` identifies the changing topology of the surfaces as a function of contour levels and extracts a series of hierarchical structures over a range of spatial scales (E. W. Rosolowsky et al. 2008). `astrodendro` was adopted with a minimum threshold of $5\sigma$ to identify structures, a minimum delta of $3\sigma$ to distinguish individual `astrodendro` leaves, and a minimum leaf size equal to the number of pixels within one synthesized beam. Across the 43 sources in our sample, a total of 125 HMFs were identified and are listed in Table B1. In parallel, we also applied `astrodendro` to the ACA+TM2 continuum to identify the associated larger structures: HMCs. These HMCs more closely resemble the definition of hot cores in the general literature. The `astrodendro` parameters used for identifying the HMCs were identical to those employed for HMFs. The designations of these HMCs are listed in column (1) of Table B1. Figure 2 provides a representative example of the identification results for both HMCs and HMFs.

Merely detecting $CH_3CN$ (12–11) lines cannot guarantee that the objects are real HMCs or HMFs; it is necessary to determine their gas temperatures. To estimate the temperatures, we applied the non–local thermodynamic equilibrium radiative transfer and spectral modeling code `SpectralRadex`[28] (F. F. S. van der Tak et al. 2007) to $CH_3CN$ (12–11) ($K$ = 0–5) spectra extracted by averaging all pixels within one beam around the identified peak of each HMF. For some sources, the $CH_3CN$ (12–11) spectra exhibit either optical thickness or blended velocity components, making it difficult to reliably constrain the kinetic temperature through spectral fitting. Thus, we excluded cases where the fitting yielded unrealistically high temperatures (>900 K, 3 times the typical hot core temperature of 300 K; H. Beuther et al. 2025). Among all the fitted sources, the calculated kinetic temperature range is from 95 to 798 K with a median value of 209 K. The kinetic temperature and other parameters of the HMFs derived from spectral fitting are listed in Table B1.

Hot cores are characterized not only by their high temperature and density but also by their chemical richness. We present four spectra of all four windows at Band 6 from representative candidates of the four categories of HMFs (see Figure 3). In addition to $CH_3CN$ (12–11) transitions, their spectra exhibit numerous other molecular emission lines. In summary, our identification of HMCs and HMFs is well

[27] http://www.dendrograms.org/

[28] https://spectralradex.readthedocs.io/en/latest/

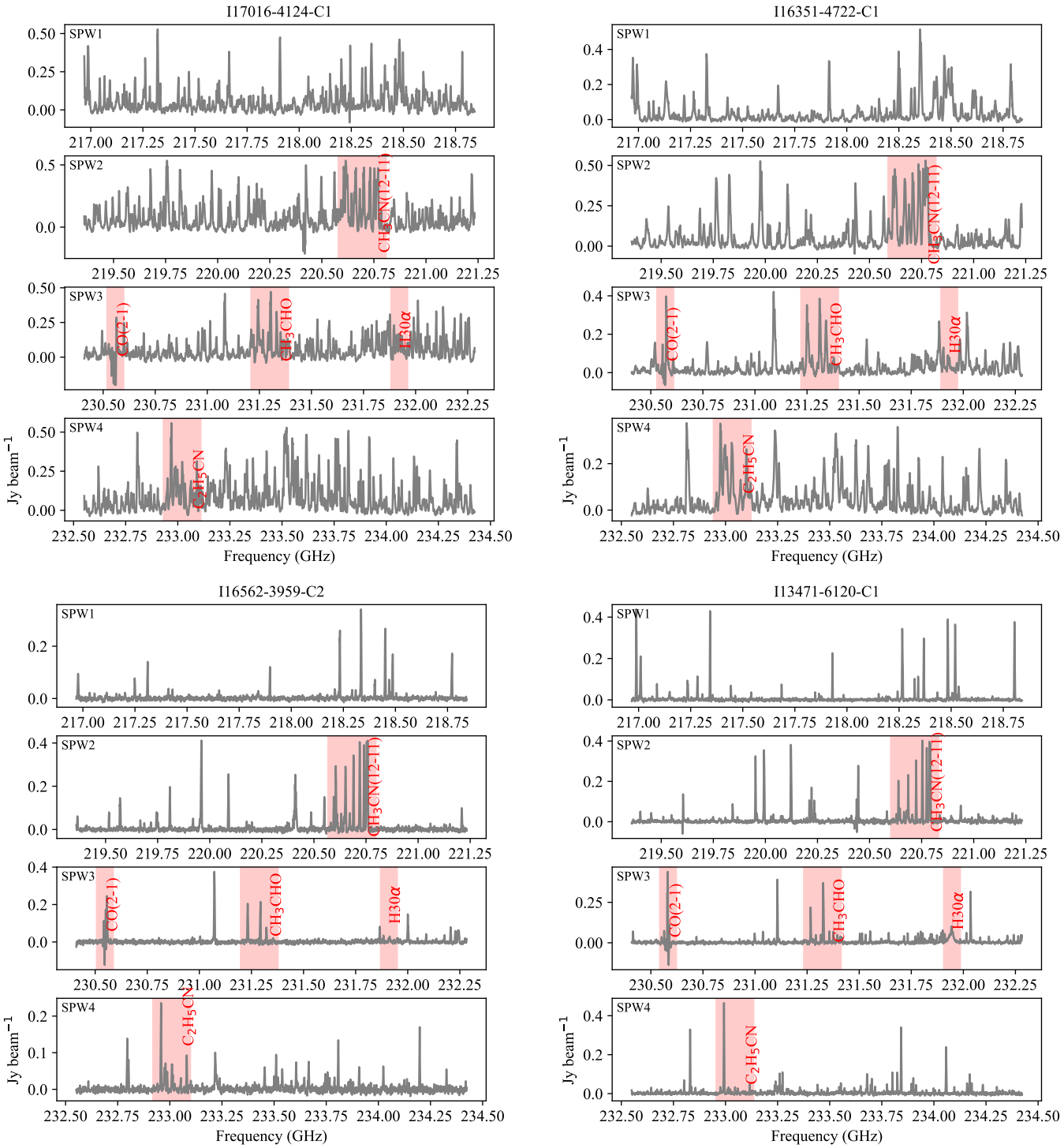


**Figure 3.** The spectra of all four windows at Band 6 at the $CH_3CN$ (12–11) emission map peaks (the positions of the white markers of Figure 1) for different kinds of HMFs. Top left panels: I17016-4124-1; top right panels: I16351-4722-1; bottom left panels: I16562-3959-2; bottom right panels: 13471-6120-1. The positions of $^{12}CO$ (2–1), $CH_3CN$ (12–11), $C_2H_5CN$ ($v = 0$), $CH_3CHO$ ($v = 0$, 1, and 2), and H30$\alpha$ are marked with red shading.

supported and consistent with the characteristics expected for chemically rich hot cores.

### 3.2. Identification of HC/UC H II Regions

Similarly, the structures of HC/UC H II region candidates (hereafter "HC/UC H II regions" for brevity) were identified using the `astrodendro` package applied to the H30$\alpha$ line integrated intensity maps with the same parameter settings as those used to identify HMFs. For 10 fields that show H30$\alpha$ nondetection, we substituted H40$\alpha$ line integrated intensity maps to identify HC/UC H II regions (giving priority to H30$\alpha$ because of its higher spatial resolution). In total, 64 HC/UC H II regions were identified and are listed in Table C1. To further classify these HC/UC H II regions, we extracted the spectra averaged over all pixels within each identified leaf and

performed Gaussian fitting to the H30$\alpha$ line. The resulting fitting parameters are provided in Table C1. For the sources without detectable H30$\alpha$ emission, we adopted the sizes and line widths derived from H40$\alpha$ instead. A visual inspection of these H40$\alpha$ structures in Figure D1 shows that the ionized regions lacking H30$\alpha$ detections are generally extended, suggesting that they may correspond to relatively more evolved UC H II regions. Following the criteria of H.-L. Liu et al. (2021), we classified the ionized structures into HC and UC H II regions based on their measured sizes and line widths (see Figure C1 and Table C1, column (12)). Specifically, we considered ionized structures with line widths greater than 40 km s$^{-1}$ and sizes smaller than 0.05 pc as candidate HC H II regions, while those with line widths between 10 and 40 km s$^{-1}$ and sizes larger than 0.05 pc were classified as candidate UC H II regions.

### 3.3. Classification of HMFs

We classify the HMFs based on their associations with HC/UC H II regions and outflows. The HMFs spatially coinciding with HC/UC H II regions are proposed to be more evolved than those without any HC/UC H II regions. Outflow collimation and morphology change with time (H. G. Arce et al. 2007), indicating that outflows can be an alternative evolutionary probe of YSOs. The youngest CO outflows are highly collimated, while more evolved outflows show wider opening angles (H. G. Arce et al. 2007). In this paper, we define spatial separation or coincidence as whether the distance between the peaks is larger than the beam size.

First of all, we clarify how the $^{12}$CO (2–1) outflow maps were obtained. We checked the $^{12}$CO (2–1) data channel by channel for each field. The different velocity ranges were selected to integrate the outflow lobes for different fields in order to avoid contamination and clearly reveal the outflow features. In the final outflow maps, we define HMFs with an outflow lobe signal-to-noise ratio greater than 5$\sigma$ as HMFs with outflows, while those with a signal-to-noise ratio below 5$\sigma$ are referred to as HMFs without detectable outflows or with very weak outflows.

The identified HMFs can be broadly classified into four categories. The first category consists of HMFs that exhibit prominent $^{12}$CO (2–1) bipolar jetlike outflows and coincide with the 1.3 mm continuum peak, such as I17016-4124-1 (shown in Figure 1). The second category consists of HMFs that show wide-angle outflows and coincide with the 1.3 mm continuum peak, such as I16351-4722-1. Note that the distinction between jetlike and wide-angle outflows is made only by visual inspection. Since there are only nine wide-angle cases, in the subsequent analysis, we combine the jetlike and wide-angle types together and refer to them as HMFs with outflows. Here we simply emphasize the existence of such a subtype of HMFs with wide angles in our sample. The third category comprises HMFs without detectable outflows or with very weak outflows but coinciding with the 1.3 mm continuum peak (such as I16562-3959-2 shown in Figure 1). The fourth category includes HMFs located around HC/UC H II regions, which lack $^{12}$CO (2–1) outflows and show a spatial separation between the $CH_3CN$ emission peak and the 1.3 mm continuum peak, such as I13471-6120-1/2 (shown in Figure 1). Additionally, these HMF types are categorized in column (14) of Table B1 as (A) jetlike outflow, 35 cores (28%); (B) wide-angle outflow, 9 cores (7%); (C) no/weak outflow, 33 cores (26%); and (D) shell-like, 48 cores (38%). (Note that not all HMFs in this category exhibit a shell-like morphology. Their common characteristic is the lack of spatial coincidence with the 1.3 mm continuum emission, rather than their specific morphology). The first three types (A, B, and C) of $CH_3CN$ emission are spatially coincident with the continuum emission, indicating that the hot molecular gas is centered on a strong compact continuum source within the fragment. These HMFs are consistent with those commonly described in other literature, in which the heating is possibly internal (candidate internally heated HMFs). In contrast, the fourth type (D) of $CH_3CN$ emission is not centered on a strong compact continuum source but rather located adjacent to one. These molecular gases are unlikely to be internally heated and are tentatively referred to here as candidate externally heated HMFs (L. A. Zapata et al. 2011). They may be residual molecular gas or newly collected gas irradiated by nearby ionized sources.

## 4. Discussion

### 4.1. Heating Mechanisms of HMFs Adjacent to HC/UC H II Regions

The shell-like HMFs are not centered on a strong, compact continuum source. If the heating were internal, the hot molecular gas would be expected to be centered on a strong, compact continuum source within the core; however, this is not the case. Instead, the observed COM ($CH_3CN$) emission appears adjacent to the continuum source. This indicates that it is unlikely to be heated from inside but rather is more consistent with being heated externally (L. A. Zapata et al. 2011).

To further investigate the heating mechanisms of these shell-like HMFs, we examined the relationship between HMF temperatures ($T_{\rm kin}$) and the H30$\alpha$ line integrated intensity ($\int IdV$) of their nearest HC/UC H II regions (Figure 4). Since the line integrated intensity is proportional to the surface H30$\alpha$ line luminosity (i.e., $\int IdV \propto L(\mathrm{H30}\alpha)/4\pi R^2$, where $R$ is the radius of the HC/UC H II region), it represents the radiative power per unit area. So the analysis in this section excludes 10 fields that have nondetectable H30$\alpha$ emission and those $CH_3CN$ that coincide with H30$\alpha$. The shell-like HMFs exhibit a statistical power-law correlation between $T_{\rm kin}$ and $\int I\,dV$, which is stronger than the nonsignificant trend observed for internally heated sources (see Figure 4). We performed a power-law fit between the HMF temperatures ($T_{\rm kin}$) and the integrated intensities of the H30$\alpha$ line using the Orthogonal Distance Regression package in scipy. In the fitting process, the uncertainties in both variables were taken into account. The best-fit power-law indices are $0.154 \pm 0.047$ for the shell-like type and $-0.024 \pm 0.038$ for the other types. This result suggests that these shell-like HMFs are likely heated by radiation from nearby HC/UC H II regions, whereas the temperature of the candidate internally heated HMFs appears to have no connection with the HC/UC H II regions located near them. L. A. Zapata et al. (2011) suggested that the "hot core" in Orion KL is primarily shock-heated. For shell-like HMFs in this work, we do not exclude the possibility of shock heating or other types of feedback. The specific feedback

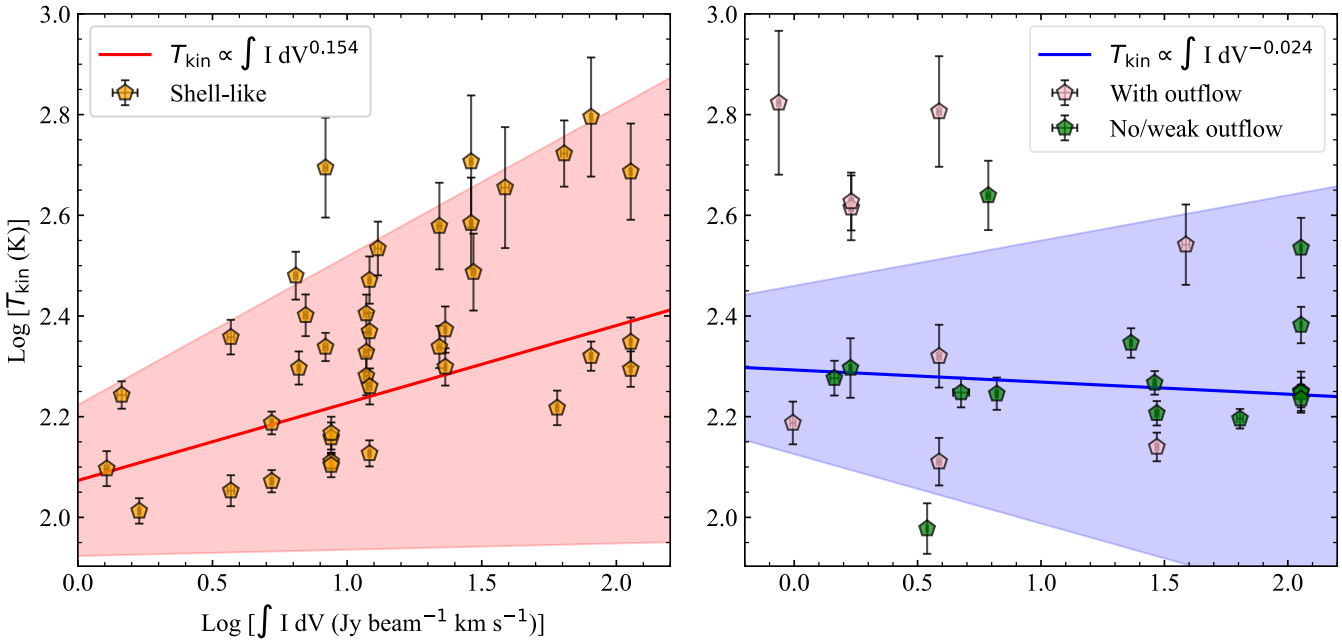


**Figure 4.** Kinetic temperature of HMFs versus H30$\alpha\int IdV$ of the nearest HC/UC H II regions. Left panel: shell-like HMFs (orange pentagons). Right panel: candidate internally heated HMFs with outflows (pink pentagons) and no/weak outflow (green pentagons). A linear regression is applied to shell-like and candidate internally heated HMFs. The corresponding relations $T_{kin} \propto \int IdV^{0.154}$ and $T_{kin} \propto \int IdV^{-0.024}$ are shown with red and blue solid lines. The red and blue shading shows 3$\sigma$ uncertainties of fitting parameters.

mechanisms likely vary from source to source and require detailed studies on individual cases.

Future investigations are underway to fully resolve the gas kinematics and temperature distributions of these shell-like (externally heated) HMFs using `spectuner`,[29] which implements the one-dimensional LTE spectral line model (Y. Qiu et al. 2025). Here, we present a `spectuner` $CH_3CN$ (12–11) fitting result for the shell-like source I13471-6120 (see Figure 5). The temperature map shows that the highest-temperature region is enclosed by the shell-like $CH_3CN$ emission, suggesting that the hot molecular gas traced by the $CH_3CN$ shell may indeed be heated by the nearby ionized region. It should be noted that the term "externally heated" here refers specifically to the HMFs (Figure 2, right panel), rather than to the larger-scale HMC associated with them (Figure 2, middle panel). Furthermore, the velocity map reveals a gradient from southeast to northwest, which is roughly aligned with the direction of the associated cometary ionized gas, indicating that this gradient is likely driven by the expansion of the ionized gas.

Therefore, consistent with the coevolutionary scenario of HMCs and HC/UC H II regions proposed in previous studies (e.g., H. Zinnecker & H. W. Yorke 2007; J. C. Tan et al. 2014; F. Motte et al. 2018), as the high-mass protostar forms, the HC/UC H II region develops but remains confined to the protostellar vicinity, embedded within the hot molecular envelope (e.g., I16562-3959-1). As the ionized gas begins to expand, it disrupts and eventually breaks through the hot molecular envelope. The expanding HC/UC H II region then compresses the disrupted molecular gas into a shell-like morphology, forming externally heated HMFs (e.g., I13471-6120-1/2).

[29] https://spectuner.readthedocs.io/en/latest/?badge=latest

### 4.2. Hot Cores Are a Long-standing Phenomenon in the Evolution of Massive Protostars

The evolutionary sequence of high-mass star formation has been extensively discussed in the literature from an observational perspective (C. R. Purcell 2006; H. Beuther et al. 2007; F. Motte et al. 2018; C. Gieser et al. 2023). In this framework, high-mass protostellar objects (HMPOs) form within massive dense cores (MDCs). These HMPOs accrete surrounding material and drive bipolar molecular outflows. As the protostar continues to heat its envelope to temperatures above 100 K, HMCs, or hot cores, develop. The massive protostar reaches the main sequence and begins emitting powerful Lyman continuum energetic enough to ionize its surroundings, leading to the formation of a hypercompact H II (HC H II) region (e.g., A. Y. Yang et al. 2019, 2021). However, whether HMCs constitute a specific evolutionary stage—i.e., a distinct, short-lived step between the HMPO and HC/UC H II phases—remains debated.

Historically, many observational studies—particularly single-dish surveys—have treated HMCs as precursors to H II regions in the high-mass star formation sequence (J. Hatchell et al. 1998; R. Cesaroni 2005; C. R. Purcell et al. 2009). These low-resolution observations of HMCs mostly exhibit smooth, elliptical morphologies (such as Figure 2, middle panel) and cannot resolve their internal substructures. Therefore, the spatial distribution of HMCs alone cannot be used to determine their specific evolutionary stage. However, high-resolution observations of these HMCs can resolve their internal structures (HMFs), whose spatial distribution (i.e., whether they are coincident with the continuum or H30$\alpha$ emission) can be used to assess whether the central object has begun to disperse its envelope (such as Figure 2, right panel). Moreover, the driving source of the outflow can be accurately located, and the outflow opening angle can then be used to

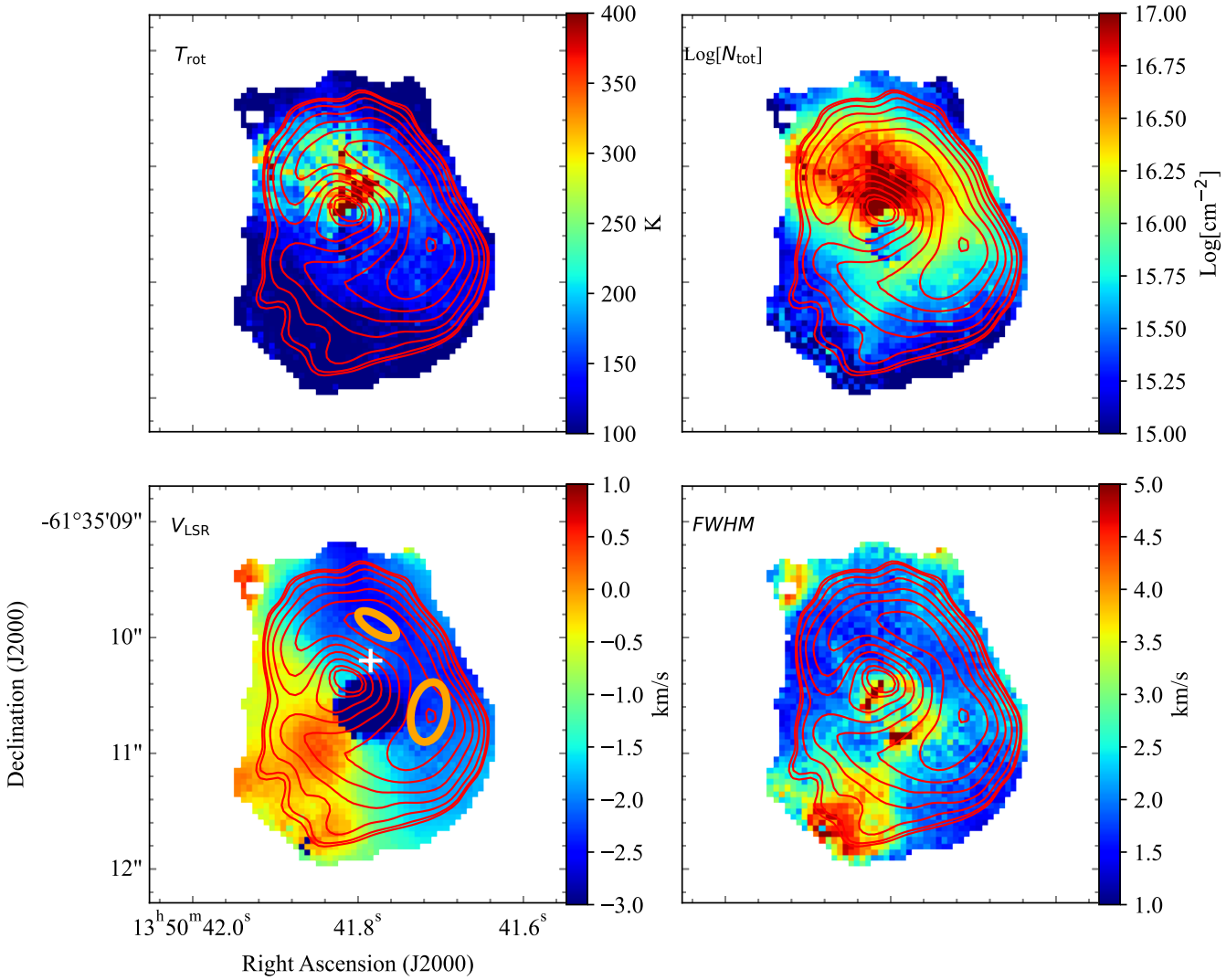


**Figure 5.** An example result from simultaneously fitting the multiple transitions of $CH_3CN$ (12–11) pixel by pixel on the I13471-6120 field using `spectuner`. Upper panels: rotational temperature (left) and maps of column density (right). Lower panels: maps of $V_{\rm LSR}$ (left; the system velocity has already been deducted) and line width (right). The red contours are the $CH_3CN$ ($12_3$–$11_3$) integrated line emission, and the levels are from $3\sigma$ to the peak intensity of the field, with eight logarithmically spaced contours between these values. In the $V_{\rm LSR}$ panel, the orange ellipses outline the structures of HMFs, and the white plus sign marks the location of the H30$\alpha$ emission peak.

infer the evolutionary stage of the embedded object (H. G. Arce et al. 2007). In our sample, these HMFs exhibit diverse characteristics, as illustrated by the examples shown in Figure 1. I17016-4124-1 exhibits a jetlike outflow and an extended hot envelope, which may be characteristic of the HMPO phase. Compared to it, I16351-4722-1 drives a wide-angle outflow, suggesting that such sources could be at the end of the HMPO stage. In I16562-3959-2, no outflow is detected, which may indicate a more evolved state. In I16562-3959-1, ionized gas appears within the inner envelope, which could signal the onset of the HC/UC H II region. Finally, in I13471-6120, the HC/UC H II region may have ionized the inner hot gas, forming shell-like structures such as I13471-6120-1 and I13471-6120-2, which could be externally heated and analogous to the "hot core" found in Orion KL (L. A. Zapata et al. 2011).

To further investigate the evolutionary sequence of candidate internally heated HMFs, we compared the sizes of HMFs with and without outflows across our sample (see the right column of Figure 6; the sizes are calculated from $CH_3CN$ ($12_3$–$11_3$) line integrated intensity maps using `astrodendro`). The Kolmogorov–Smirnov (K-S) test ($p$-value $= 0.0002 \ll 0.003$) reveals a statistically significant difference between HMF sizes with and without outflows. In addition, the Anderson–Darling (A-D) test, which evaluates whether a sample comes from a specified distribution by giving more weight to the tails, was also performed for the HMF sizes with and without outflows, yielding a significance level of $p$-value $= 0.005$. We find that HMFs without outflows have slightly smaller sizes (median FWHM $\simeq 1500 \pm 420$ au) than those with outflows (median FWHM $\simeq 3000 \pm 440$ au). To eliminate potential distance effects on the above conclusion, we examined the correlation between the $CH_3CN$ ($12_3$–$11_3$) line integrated intensity of all HMFs and their distances. A Pearson correlation test yields $r = -0.038$ with a $p$-value of 0.67, indicating no statistically significant correlation. This result confirms that distance does not bias our findings.

Compared to low-resolution observations, high-resolution data resolve the internal structures of HMCs and accurately

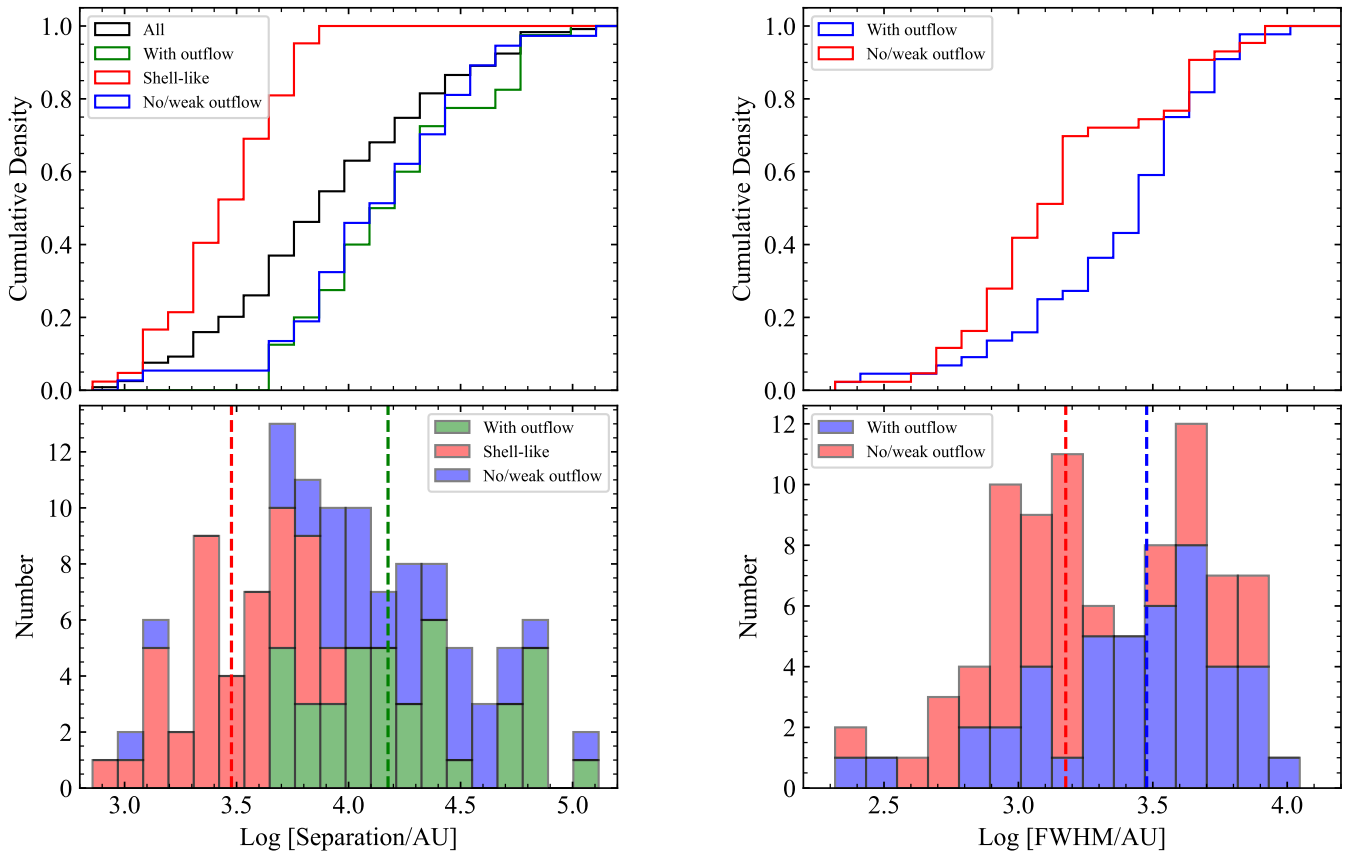


**Figure 6.** Left column: histogram (bottom) and cumulative density distribution (top) for the separation between different kinds of HMFs and the nearest HC/UC H II regions. For the shell-like type, the nearest HC/UC H II region is defined as the HC/UC H II region enclosed by the nearby $CH_3CN$ emission, whereas for the other types, the nearest HC/UC H II region is taken to be the closest HC/UC H II region within the entire image (Figure D1). The red and green vertical dashed lines indicate the median value of externally (shell-like) and internally (with and without outflow) heated candidate HMFs, respectively. The separation is calculated using the distance from X. Liu et al. (2024) and the intensity peak coordinates of Tables B1 and C1. Right column: histogram (bottom) and cumulative density distribution (top) for the FWHMs ($=\sqrt{\text{Maj\_FWHM} \times \text{Min\_FWHM}} \times$ distance) of different kinds of HMFs. The red and blue vertical dashed lines indicate the corresponding median value.

locate the outflows driven by the embedded objects. We therefore suggest that it is necessary to reconsider the HMC phase within the evolutionary sequence of high-mass protostars. According to the previously proposed evolutionary scenario (e.g., H. Zinnecker & H. W. Yorke 2007; J. C. Tan et al. 2014; F. Motte et al. 2018), we present the possible characteristics of the HMC phase as illustrated in Figure 7. For completeness, we depict the entire evolutionary sequence of high-mass star formation, including the earlier hub–filament system phase (e.g., F.-W. Xu et al. 2023; D. Berdikhan et al. 2025; D. Meng et al. 2025). We divide the HMC phase into four classes: phase 0, characterized by jetlike outflows and hot core envelopes (e.g., I17016-4124-1); phase I, exhibiting wide-angle outflows (e.g., I16351-4722-1) or lacking detectable outflows (e.g., 16562-3959-1/2), still with hot molecular envelopes; phase II, associated with HC/UC H II regions and hot molecular shells (e.g., I13471-6120-1/2); and phase III, showing HC/UC H II regions without any detectable hot molecular envelopes. It should be noted that this cartoon illustrates the evolutionary path of most high-mass protostars. In several sources from our sample, an HC/UC H II region has already formed, yet a bipolar outflow is still being driven. These exceptional cases are not illustrated in the cartoon. This sequence is our current best interpretation using both our data and the current literature and provides new insights of exploration for evolutionary models of massive star formation.

In summary, hot cores could be a long-standing phenomenon in the evolution of massive protostars. They can appear as very young protostars with outflows, evolved protostars without outflows, or externally heated shells.

### *4.3. Implications for Stellar Feedback within Young Protoclusters*

H.-L. Liu et al. (2021) identified through the ATOMS survey that 12% (53/453) of compact dense cores simultaneously host HC/UC H II regions and COM emission. Notably, within these sources, hot cores were found to persist for over half of the lifetime of the HC/UC H II regions, even after the central objects had begun ionizing their surroundings. However, due to the limited angular resolution of ATOMS, it remained unclear whether these COM emissions originated from residual shell gas located near the HC/UC H II regions or a genuine internally heated hot core at a distinct evolutionary stage (I. Jimenez-Serra et al. 2025).

Since this section focuses on the spatial separations between $CH_3CN$ emission and H30$\alpha$/H40$\alpha$ emission, we explicitly exclude the sources in which $CH_3CN$ emission is spatially

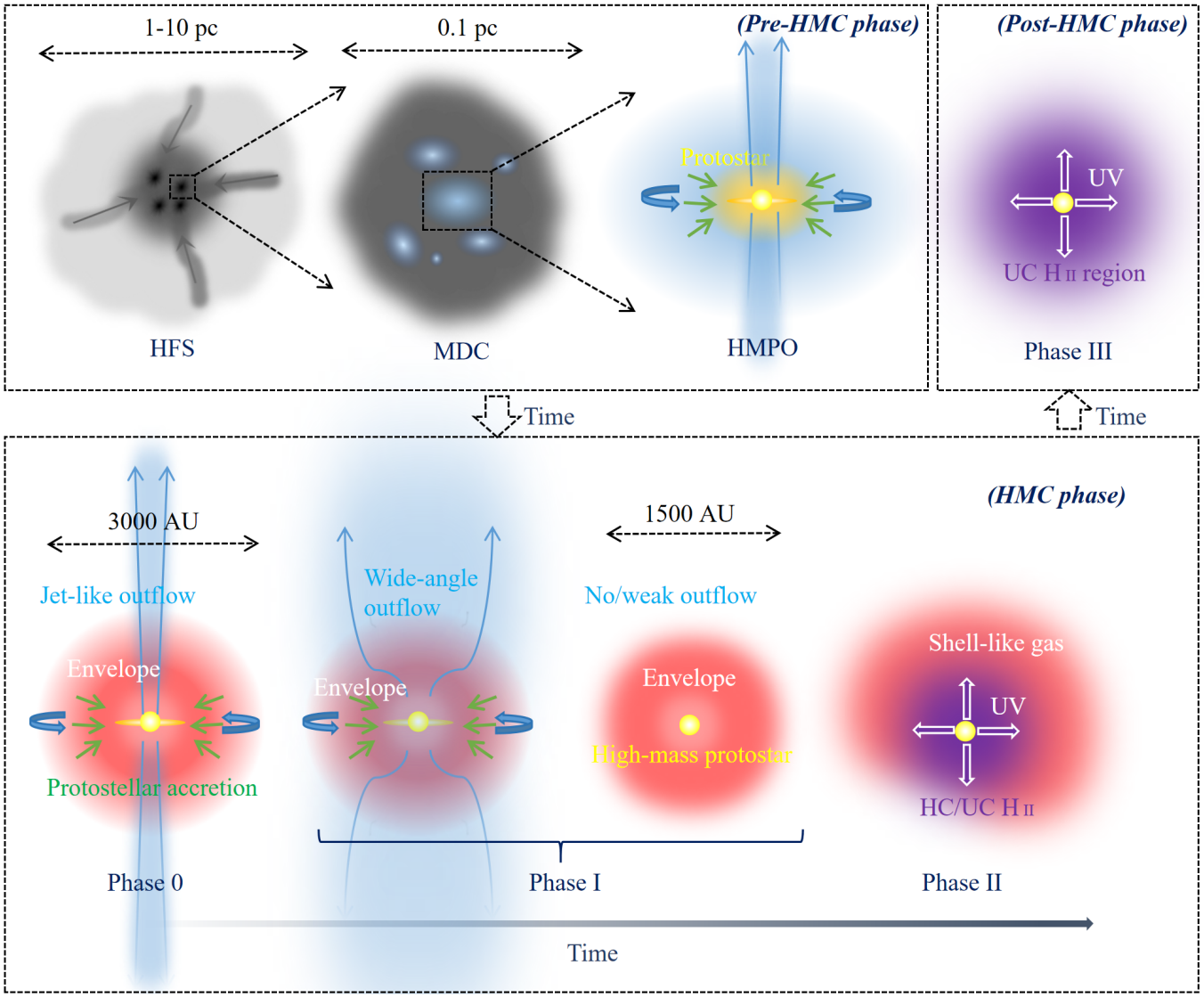


**Figure 7.** An illustrated overview of high-mass protostellar evolutionary classes. HFS: hub–filament system, the primary birthplace of massive stars. The MDC is formed via fragmentation in the hub, and the center undergoes further internal fragmentation to produce multiple prestellar cores. The HMPO is with jetlike outflow and without a hot molecular envelope. Phase 0, jetlike outflow and hot molecular envelope (e.g., I17016-4124-1); phase I, wide-angle outflow (e.g., I16351-4722-1) or no outflow (e.g., I16562-3959-2) and hot molecular envelope; phase II, HC/UC H II and shell-like HMFs (e.g., 13471-6120-1/2); phase III, HC/UC H II without hot molecular envelope. Gray, blue, red, and purple represent cold ($\lesssim$20 K), warm (20$\sim$100 K), hot ($\gtrsim$100 K), and ionized regions, respectively.

coincident with the H30$\alpha$/H40$\alpha$ emission. The definitions of separation and coincidence are provided in Section 3.3.

Our QUARKS sample offers sufficient resolution ($\sim$0.″3, $\sim$1300 au at the median distance 4.76 kpc of our sample) to resolve COM emission adjacent to the HC/UC H II regions. We find that these COMs around HC/UC H II regions consist of two distinct types: externally heated, shell-like HMFs (associated with adjacent HC/UC H II regions, forming phase II) and candidate internally heated HMFs (including phase 0 and phase I). For the latter case, it is important to assess whether their formation has been triggered by the nearest HC/UC H II region through the "collect-and-collapse" process, in which stellar feedback from massive stars strongly influences the nearby ISM and regulates subsequent star formation. Specifically, the expansion of an HC/UC H II region can sweep up the ambient molecular gas into a dense shell, which may eventually become gravitationally unstable and fragment to form new stars (B. G. Elmegreen & C. J. Lada 1977; A. P. Whitworth et al. 1994). Alternatively, these HMFs may simply represent independent star-forming sites that happen to be located nearby, having originated from the fragmentation of a common parental clump but evolving at different rates. However, for the candidate internally heated HMFs, we found no evidence of interplay with the nearby HC/UC H II regions. The separation between these candidate internally heated HMFs and their nearest HC/UC H II regions is 15,000 $\pm$ 3600 au (median value), which is significantly larger than the 3000 $\pm$ 380 au (median value) separation observed for the shell-like HMFs (as shown in Figure 6, left column). Furthermore, the A-D ($p$-value $< 0.001$) and K-S ($p$-value $< 0.001$) tests indicate that the separations between shell-like HMFs and nearby HC/UC H II regions (red line in Figure 6, left column) and those between candidate internally heated HMFs and nearby HC/UC H II regions (black and green lines in Figure 6, left column) are drawn from different distributions. Assuming the observed separation for candidate internally heated HMFs is attributed to feedback from HC/UC H II regions, the

dynamical timescale of the HC/UC H II regions can be estimated at $t_{\rm dyn} \sim \frac{\rm Separation}{V_S} \lesssim \frac{15,000\ {\rm au}}{10\ {\rm km\ s^{-1}}} < 1 \times 10^4$ yr (T. Liu et al. 2017). However, this is significantly shorter than the lifetime of high-mass prestellar cores ($\sim$1–7 $\times$ $10^4$ yr; F. Motte et al. 2018) or IR-quiet high-mass protostars ($\sim$2 $\times$ $10^5$ yr; F. Motte et al. 2018), which are precursors before developing HMCs, suggesting that HC/UC H II feedback alone cannot fully explain the formation and evolution of these candidate internally heated HMFs.

We propose that the separations between these candidate internally heated HMFs and the HC/UC H II regions are likely governed by turbulent or thermal fragmentation processes (T. Liu et al. 2017). The separations between the majority of the candidate internally heated HMFs and the nearest HC/UC H II regions span 4000–60,000 au, covering the characteristic fragmentation scales observed across low-mass ($\sim$20,000 au), intermediate-mass ($\sim$6000 au), and high-mass ($\sim$4000 au) regions as reported in H. Beuther et al. (2025). Therefore, sequential high-mass star formation within young protoclusters could result primarily from the fragmentation of the parental clump, rather than being triggered by feedback mechanisms.

## 5. Conclusions

We present high-resolution images of protoclusters from the QUARKS survey. These images simultaneously reveal $CH_3CN$ emission and H30$\alpha$/H40$\alpha$ emission. By combining CO outflow and 1.3 mm continuum, we find that the $CH_3CN$-detected structures (HMFs) can be grouped into categories associated with jetlike outflows, wide-angle outflows, no/weak outflows, and shell-like morphologies. These HMFs represent the substructures of HMCs, and such classification provides further insight into the nature of HMCs—a long-standing phenomenon in the evolution of massive protostars.

These images also allow us to resolve $CH_3CN$ emission in the vicinity of the H30$\alpha$/H40$\alpha$ regions. We find $CH_3CN$ emission near the ionized gas in two distinct configurations: residual molecular gas adjacent to the ionized region and a separate source at a different evolutionary stage. An analysis of the projected separations shows that the former has a median distance of $\sim$3000 au, while the latter has a larger median distance of $\sim$15,000 au, suggesting that the latter sources may not be physically related to the nearby HC/UC H II region.

## Acknowledgments

We thank the referee for providing constructive comments that substantially improved the quality of the paper. This work was main funded by the National Key R&D Program of China under grant Nos. 2022YFA1603100 and 2023YFA1608002 and Tianshan Talent Training Program 2024TSYCTD0013. It was also partially funded by the NSFC under grants 12173075, 12373029 and 12403033, the CAS Light of West China Program XBZG-ZDSYS-202212, the Tianshan Talent Program of Xinjiang Uygur Autonomous Region under grant No. 2022TSYCLJ0005, and the Youth Innovation Promotion Association CAS. T.L. acknowledges the support by the National Natural Science Foundation of China (NSFC) through grants No. 12073061 and No. 12122307, the PIFI program of the Chinese Academy of Sciences through grant No. 2025PG0009, and the Tianchi Talent Program of Xinjiang Uygur Autonomous Region. S.-L.Q. is supported by NSFC under No. 12033005. This work was performed in part at the Jet Propulsion Laboratory, California Institute of Technology, under contract with the National Aeronautics and Space Administration (80NM0018D0004); G.G. and L.B. gratefully acknowledge support by the ANID BASAL project FB210003; S.R.D. acknowledges support from the Fondecyt Postdoctoral fellowship (project code 3220162) and ANID BASAL project FB210003; P.S. was partially supported by a Grant-in-Aid for Scientific Research (KAKENHI number JP23H01221) of JSPS; and N.K.B. acknowledges the support of the China Postdoctoral Science Foundation through grant No. 2025M773187. G.W. acknowledges the support from the Xinjiang Tianchi Talent Program. The Central Guidance for Local Science and Technology Development Fund ZYYD2025ZY23.

*Facility:* ALMA

*Software:* Astropy (Astropy Collaboration et al. 2022), CASA (CASA Team et al. 2022), CARTA (A. Comrie et al. 2021), Astrodendro (E. W. Rosolowsky et al. 2008), RADEX (F. F. S. van der Tak et al. 2007), Spectuner (Y. Qiu et al. 2025).

## Appendix A
## The Sample Selected from the QUARKS Survey

In this section, we present the basic parameters of 43 fields in Table A1, including source IDs in our sample (column (1)), IRAS names (column (2)), coordinates (columns (3) and (4)), systemic velocities ($V_{\rm LSR}$; column (5)), distances from the Sun (column (6)), galactocentric distances ($R_{\rm GC}$; column (7)), effective radius (column (8)), dust temperature ($T_{\rm dust}$; column (9)), bolometric luminosity ($L_{\rm bol}$; column (10)), and clump masses ($M_{\rm clump}$; column (11)).

**Table A1**
The Basic Information of 43 Fields in Our Sample

| ID | Target | Glon (deg) | Glat (deg) | $V_{LSR}$ (km s$^{-1}$) | Distance (kpc) | $R_{GC}$ (kpc) | Radius (pc) | $T_{dust}$ (K) | log($L_{bol}$) ($L_{\odot}$) | log($M_{clump}$) ($M_{\odot}$) |
|---|---|---|---|---|---|---|---|---|---|---|
| (1) | (2) | (3) | (4) | (5) | (6) | (7) | (8) | (9) | (10) | (11) |
| 1 | I12320-6122 | 300.96916 | 1.14564 | −43.2 | 4.17 | 7.2 | 1.00 | 44.6 | 5.6 | 3.0 |
| 2 | I12326-6245 | 301.13583 | −0.22582 | −39.5 | 4.21 | 7.2 | 0.83 | 34.2 | 5.4 | 3.5 |
| 3 | I12572-6316_1 | 303.93008 | −0.68782 | 30.4 | 11.63 | 9.8 | 1.63 | 21.5 | 4.6 | 3.9 |
| 4 | I13471-6120 | 309.92084 | 0.47748 | −57.8 | 5.17 | 6.4 | 1.01 | 35.1 | 5.3 | 3.4 |
| 5 | I15254-5621 | 323.45906 | −0.07914 | −68.6 | 4.42 | 5.7 | 0.89 | 33.5 | 5.1 | 3.1 |
| 6 | I15290-5546 | 324.20074 | 0.12008 | −88.3 | 7.94 | 4.9 | 1.80 | 33.5 | 5.7 | 3.8 |
| 7 | I15411-5352 | 326.72494 | 0.61576 | −41.8 | 2.41 | 6.9 | 0.57 | 30.5 | 4.5 | 2.7 |
| 8 | I15439-5449 | 326.47310 | −0.37656 | −54.8 | 3.40 | 5.9 | 0.69 | 26.8 | 4.4 | 3.0 |
| 9 | I15502-5302 | 328.30750 | 0.43085 | −92.4 | 5.49 | 4.6 | 1.66 | 35.7 | 5.8 | 3.7 |
| 10 | I15520-5234 | 328.80764 | 0.63243 | −41.8 | 2.56 | 6.2 | 0.67 | 32.2 | 5.1 | 3.2 |
| 11 | I15567-5236 | 329.33743 | 0.14749 | −107.5 | 5.22 | 4.4 | 1.31 | 35.4 | 5.7 | 3.5 |
| 12 | I16037-5223 | 330.29433 | −0.39406 | −81.3 | 9.04 | 4.9 | 2.15 | 31.4 | 5.6 | 3.8 |
| 13 | I16060-5146 | 330.95419 | −0.18248 | −92.1 | 5.39 | 4.5 | 1.24 | 32.2 | 5.8 | 3.9 |
| 14 | I16065-5158 | 330.87788 | −0.36624 | −62.5 | 4.33 | 5.2 | 1.41 | 30.8 | 5.4 | 3.7 |
| 15 | I16071-5142 | 331.13062 | −0.24240 | −86.5 | 5.29 | 4.5 | 1.21 | 23.9 | 4.8 | 3.7 |
| 16 | I16164-5046 | 332.82560 | −0.54900 | −56.7 | 4.02 | 5.4 | 1.37 | 31.4 | 5.5 | 3.7 |
| 17 | I16172-5028_1 | 333.13502 | −0.43180 | −53.3 | 3.78 | 5.4 | 1.51 | 32.0 | 5.8 | 4.0 |
| 18 | I16313-4729 | 336.86551 | 0.00213 | −74.1 | 4.99 | 4.4 | 2.06 | 31.0 | 6.7 | 4.7 |
| 19 | I16348-4654 | 337.70403 | −0.05342 | −47.8 | 11.33 | 5.4 | 2.40 | 23.6 | 5.4 | 4.4 |
| 20 | I16351-4722 | 337.40474 | −0.40206 | −40.8 | 2.33 | 5.7 | 0.69 | 30.4 | 4.9 | 3.2 |
| 21 | I16445-4459 | 340.24917 | −0.04582 | −122.2 | 7.72 | 2.8 | 2.54 | 24.6 | 5.0 | 3.9 |
| 22 | I16458-4512 | 340.24749 | −0.37413 | −50.9 | 4.19 | 5.1 | 1.42 | 21.4 | 4.5 | 3.6 |
| 23 | I16562-3959 | 345.49528 | 1.47062 | −11.3 | 1.37 | 6.1 | 0.72 | 42.3 | 5.7 | 3.2 |
| 24 | I17016-4124 | 345.00285 | −0.22408 | −26.8 | 3.16 | 7.0 | 0.75 | 32.0 | 5.3 | 3.8 |
| 25 | I17143-3700 | 350.01583 | 0.43248 | −31.7 | 11.71 | 4.7 | 2.95 | 31.0 | 5.6 | 3.8 |
| 26 | I17160-3707 | 350.10365 | 0.08132 | −69.4 | 10.28 | 2.7 | 1.69 | 28.5 | 6.0 | 4.1 |
| 27 | I17175-3544 | 351.41758 | 0.64492 | −8.7 | 1.32 | 7.0 | 0.35 | 30.6 | 4.8 | 3.1 |
| 28 | I17204-3636 | 351.04114 | −0.33570 | −18.1 | 3.27 | 5.1 | 0.60 | 25.8 | 4.2 | 2.9 |
| 29 | I17220-3609 | 351.58185 | −0.35181 | −97.2 | 8.05 | 1.3 | 2.41 | 25.4 | 5.7 | 4.3 |
| 30 | I17271-3439_1 | 353.40990 | −0.36021 | −17.2 | 3.66 | 5.3 | 1.34 | 35.0 | 5.6 | 4.0 |
| 31 | I17545-2357 | 5.63735 | 0.23748 | 8.8 | 3.00 | 5.4 | 0.87 | 23.7 | 4.1 | 3.1 |
| 32 | I17599-2148 | 8.14078 | 0.22409 | 18.6 | 3.44 | 5.4 | 1.15 | 32.0 | 5.2 | 3.4 |
| 33 | I18032-2032 | 9.61969 | 0.19657 | 4.4 | 4.80 | 3.4 | 1.27 | 32.1 | 5.4 | 3.5 |
| 34 | I18056-1952 | 10.47249 | 0.02752 | 66.4 | 8.44 | 1.6 | 2.32 | 25.1 | 5.7 | 4.4 |
| 35 | I18110-1854 | 11.93713 | −0.61570 | 38.5 | 3.17 | 5.1 | 0.87 | 28.9 | 4.8 | 3.2 |
| 36 | I18116-1646 | 13.87386 | 0.28067 | 48.8 | 3.86 | 4.6 | 0.99 | 33.8 | 5.1 | 3.1 |
| 37 | I18434-0242 | 29.95723 | −0.01729 | 97.5 | 4.76 | 4.7 | 1.48 | 35.5 | 5.7 | 3.6 |
| 38 | I18469-0132 | 31.39533 | −0.25773 | 86.6 | 4.91 | 4.7 | 0.68 | 32.2 | 4.8 | 3.0 |
| 39 | I18479-0005 | 32.79860 | 0.18954 | 14.6 | 12.87 | 7.5 | 2.45 | 34.2 | 6.1 | 4.2 |
| 40 | I18507+0110 | 34.25691 | 0.15530 | 58.2 | 3.23 | 7.1 | 0.44 | 29.2 | 4.8 | 3.2 |
| 41 | I19078+0901 | 43.16581 | 0.01086 | 6.2 | 11.49 | 7.6 | 4.26 | 33.3 | 6.9 | 5.0 |
| 42 | I19095+0930 | 43.79414 | −0.12749 | 43.8 | 9.07 | 5.8 | 0.64 | 34.9 | 5.1 | 3.1 |
| 43 | I19097+0847 | 43.17804 | −0.51881 | 58.2 | 7.83 | 6.2 | 2.01 | 23.3 | 5.0 | 3.8 |

## Appendix B
## Hot Core Catalog

All HMFs identified using `astrodendro` are listed in Table B1. Columns (1)–(9) are their corresponding larger-scale HMC ID, HMF ID, $CH_3CN$ ($12_3$–$11_3$) line integrated intensity peak coordinates R.A. and decl., major FWHM and minor FWHM in arcseconds, major FWHM and minor FWHM in au, and position angle measured from north to east. Columns (10)–(13) list the line-of-sight velocities, line widths, and kinetic temperatures and their uncertainties, as well as the $CH_3CN$ column densities and their uncertainties. Rows with hyphens indicate sources for which the $CH_3CN$ fitting yielded $T_{kin} > 900$ K. Since we regard such values as unreliable, these fits were discarded and not considered in the analysis presented in Section 4.1. This cutoff of 900 K is adopted because HMCs in the high-mass star formation phase typically have temperatures of about 300 K (H. Beuther et al. 2025). We therefore adopted 3 times this characteristic value as a tolerance threshold.

**Table B1**
Physical Parameters of the HMFs

| Core | Fragment | R.A. (deg) | Decl. (deg) | Maj_FWHM (arcsec) | Min_FWHM (arcsec) | Maj_size (au) | Min_size (au) | PA (deg) | Vlsr (km s$^{-1}$) | Line Width (km s$^{-1}$) | $T_{\rm kin}$ (K) | ERR$_T$ (K) | Flag[a] |
|---|---|---|---|---|---|---|---|---|---|---|---|---|---|
| (1) | (2) | (3) | (4) | (5) | (6) | (7) | (8) | (9) | (10) | (11) | (12) | (13) | (14) |
| I12320-6122-C1 | 1 | 188.72195 | −61.66142 | 0.55 | 0.31 | 2302 | 1301 | −152 | −43.55 | 5.35 | 176 | 13 | C |
| I12320-6122-C1 | 2 | 188.72171 | −61.66103 | 0.89 | 0.46 | 3703 | 1902 | 109 | −36.96 | 3.55 | 198 | 15 | D |
| I12326-6245-C1 | 1 | 188.89608 | −63.04233 | 0.48 | 0.24 | 2021 | 1010 | 174 | −39.35 | 3.41 | 223 | 25 | D |
| I12326-6245-C1 | 2 | 188.89688 | −63.04206 | 0.43 | 0.29 | 1819 | 1212 | 82 | −39.01 | 3.28 | 178 | 16 | C |
| I12326-6245-C1 | 3 | 188.89633 | −63.04206 | 0.82 | 0.36 | 3435 | 1516 | −151 | −38.94 | 5.67 | 486 | 107 | D |
| I12326-6245-C1 | 4 | 188.89682 | −63.04181 | 0.53 | 0.24 | 2223 | 1010 | 60 | −37.67 | 4.44 | 197 | 16 | D |
| I12326-6245-C1 | 5 | 188.89587 | −63.04179 | 0.22 | 0.17 | 909 | 707 | 98 | −44.24 | 5.51 | 343 | 47 | C |
| I12326-6245-C1 | 6 | 188.89749 | −63.04174 | 0.34 | 0.26 | 1415 | 1111 | 140 | −38.22 | 5.68 | 241 | 20 | C |
| I12326-6245-C1 | 7 | 188.89614 | −63.04162 | 0.19 | 0.12 | 808 | 505 | 165 | −41.15 | 3.92 | 177 | 12 | C |
| I12326-6245-C1 | 8 | 188.89559 | −63.04117 | 0.31 | 0.26 | 1314 | 1111 | 131 | −40.42 | 4.75 | 172 | 11 | C |
| I12572-6316_1-C1 | 1 | 195.10084 | −63.54217 | 0.22 | 0.19 | 2512 | 2233 | 102 | 31.84 | 6.12 | 154 | 15 | A |
| I13471-6120-C1 | 1 | 207.67381 | −61.58629 | 0.50 | 0.29 | 2606 | 1489 | 78 | −60.20 | 3.71 | 218 | 14 | D |
| I13471-6120-C1 | 2 | 207.67407 | −61.58608 | 0.36 | 0.14 | 1861 | 744 | 149 | −60.14 | 3.12 | 495 | 113 | D |
| I15254-5621-C1 | 1 | 232.33054 | −56.52287 | 0.79 | 0.26 | 3501 | 1167 | 84 | −66.77 | 3.94 | 379 | 75 | D |
| I15254-5621-C1 | 2 | 232.33046 | −56.52251 | 0.53 | 0.31 | 2334 | 1379 | 96 | −69.38 | 2.59 | 218 | 21 | D |
| I15290-5546-C1 | 1 | 233.22023 | −55.93535 | 0.91 | 0.74 | 7241 | 5907 | 56 | −88.44 | 7.99 | 412 | 61 | A |
| I15290-5546-C1 | 2 | 233.21956 | −55.93518 | 0.38 | 0.36 | 3049 | 2858 | 73 | −90.66 | 7.88 | 424 | 56 | A |
| I15411-5352-C1 | 1 | 236.24839 | −54.03960 | 0.53 | 0.48 | 1272 | 1157 | 145 | −41.68 | 10.80 | 666 | 219 | A |
| I15439-5449-C1 | 1 | 236.95741 | −54.97669 | 0.86 | 0.50 | 2938 | 1714 | 121 | −53.47 | 9.66 | 209 | 31 | A |
| I15502-5302-C1 | 1 | 238.52730 | −53.19496 | 0.17 | 0.17 | 922 | 922 | 102 | −88.25 | 2.60 | 144 | 10 | D |
| I15502-5302-C1 | 2 | 238.52753 | −53.19479 | 0.77 | 0.41 | 4216 | 2240 | 118 | −92.04 | 5.31 | 129 | 4 | D |
| I15502-5302-C1 | 3 | 238.52656 | −53.19485 | 0.34 | 0.12 | 1845 | 659 | 172 | −92.04 | 3.80 | 127 | 7 | D |
| I15502-5302-C1 | 4 | 238.52668 | −53.19475 | 0.19 | 0.14 | 1054 | 791 | 63 | −92.21 | 4.57 | 147 | 11 | D |
| I15520-5234-C1 | 1 | 238.95234 | −52.71864 | 0.41 | 0.29 | 1044 | 737 | 119 | −41.86 | 4.20 | 296 | 32 | D |
| I15520-5234-C1 | 2 | 238.95197 | −52.71858 | 0.58 | 0.46 | 1475 | 1167 | 83 | −43.53 | 4.32 | 234 | 20 | D |
| I15520-5234-C2 | 3 | 238.95073 | −52.71835 | 0.62 | 0.34 | 1597 | 860 | 140 | −42.84 | 2.95 | 113 | 8 | D |
| I15520-5234-C1 | 4 | 238.95266 | −52.71837 | 0.53 | 0.29 | 1352 | 737 | 155 | −40.65 | 4.44 | 166 | 8 | C* |
| I15520-5234-C1 | 5 | 238.95344 | −52.71824 | 0.53 | 0.29 | 1352 | 737 | 97 | −41.98 | 2.84 | 118 | 6 | D |
| I15520-5234-C2 | 6 | 238.95185 | −52.71824 | 0.22 | 0.14 | 553 | 369 | 76 | −44.18 | 1.91 | 228 | 18 | D |
| I15520-5234-C1 | 7 | 238.95291 | −52.71818 | 0.29 | 0.24 | 737 | 614 | −177 | −42.54 | 5.26 | 154 | 8 | D |
| I15520-5234-C1 | 8 | 238.95224 | −52.71803 | 0.22 | 0.17 | 553 | 430 | 48 | −43.50 | 2.39 | 134 | 8 | D |
| I15567-5236-C1 | 1 | 240.13783 | −52.74604 | 0.31 | 0.29 | 1629 | 1503 | 92 | −113.31 | 4.71 | 177 | 20 | C* |
| I15567-5236-C1 | 2 | 240.13804 | −52.74444 | 0.24 | 0.19 | 1253 | 1002 | −138 | −107.11 | 2.41 | 95 | 11 | C |
| I16037-5223-C1 | 1 | 241.90930 | −52.51721 | 0.50 | 0.48 | 4556 | 4339 | −141 | - | - | - | - | C |
| I16037-5223-C1 | 2 | 241.90884 | −52.51721 | 0.46 | 0.31 | 4122 | 2820 | 127 | −78.62 | 13.46 | 209 | 30 | A |
| I16037-5223-C1 | 3 | 241.90836 | −52.51704 | 0.65 | 0.34 | 5858 | 3037 | −156 | −79.00 | 9.02 | 640 | 162 | A |
| I16037-5223-C1 | 4 | 241.90918 | −52.51681 | 0.31 | 0.26 | 2820 | 2387 | 94 | −80.56 | 7.68 | 129 | 14 | A |
| I16060-5146-C2 | 1 | 242.46818 | −51.91606 | 0.41 | 0.22 | 2199 | 1164 | 109 | −88.34 | 2.86 | 129 | 5 | C* |
| I16060-5146-C1 | 2 | 242.46922 | −51.91586 | 0.43 | 0.31 | 2328 | 1682 | −148 | −89.00 | 4.00 | 185 | 10 | C |
| I16060-5146-C1 | 3 | 242.46852 | −51.91557 | 1.10 | 0.58 | 5951 | 3105 | 60 | - | - | - | - | A |
| I16060-5146-C1 | 4 | 242.46962 | −51.91550 | 0.22 | 0.17 | 1164 | 906 | 98 | −95.97 | 5.54 | 384 | 80 | D |
| I16060-5146-C1 | 5 | 242.46915 | −51.91525 | 0.46 | 0.24 | 2458 | 1294 | 157 | −94.23 | 7.62 | 509 | 154 | D |
| I16060-5146-C1 | 6 | 242.46834 | −51.91519 | 0.29 | 0.12 | 1552 | 647 | 73 | −86.01 | 4.30 | 342 | 42 | D |
| I16060-5146-C1 | 7 | 242.46971 | −51.91517 | 0.26 | 0.10 | 1423 | 517 | 84 | - | - | - | - | D |
| I16060-5146-C1 | 8 | 242.46962 | −51.91490 | 0.55 | 0.26 | 2975 | 1423 | 74 | −95.62 | 5.87 | 624 | 170 | D |
| I16060-5146-C2 | 9 | 242.46845 | −51.91482 | 0.96 | 0.70 | 5174 | 3751 | 165 | - | - | - | - | D |

**Table B1**
(Continued)

| Core | Fragment | R.A. (deg) | Decl. (deg) | Maj_FWHM (arcsec) | Min_FWHM (arcsec) | Maj_size (au) | Min_size (au) | PA (deg) | Vlsr (km s$^{-1}$) | Line Width (km s$^{-1}$) | $T_{kin}$ (K) | ERR$_T$ (K) | Flag[a] |
|---|---|---|---|---|---|---|---|---|---|---|---|---|---|
| (1) | (2) | (3) | (4) | (5) | (6) | (7) | (8) | (9) | (10) | (11) | (12) | (13) | (14) |
| I16060-5146-C1 | 10 | 242.46926 | −51.91464 | 0.38 | 0.19 | 2070 | 1035 | −154 | −93.95 | 6.40 | 209 | 14 | D |
| I16065-5158-C1 | 1 | 242.58309 | −52.10344 | 0.41 | 0.24 | 1767 | 1039 | 179 | - | - | - | - | C |
| I16065-5158-C1 | 2 | 242.58257 | −52.10335 | 0.72 | 0.19 | 3118 | 831 | −139 | - | - | - | - | C |
| I16065-5158-C2 | 3 | 242.58296 | −52.10211 | 2.02 | 1.68 | 8729 | 7274 | 123 | - | - | - | - | A |
| I16071-5142-C1 | 1 | 242.74909 | −51.84012 | 0.38 | 0.19 | 2031 | 1016 | 102 | −83.68 | 6.48 | 243 | 20 | C |
| I16071-5142-C1 | 2 | 242.74893 | −51.83967 | 1.08 | 0.74 | 5713 | 3936 | 83 | - | - | - | - | A |
| I16164-5046-C1 | 1 | 245.04601 | −50.88833 | 0.65 | 0.48 | 2604 | 1929 | 61 | - | - | - | - | A |
| I16164-5046-C1 | 2 | 245.04605 | −50.88765 | 1.54 | 1.15 | 6173 | 4630 | 115 | - | - | - | - | A |
| I16164-5046-C1 | 3 | 245.04528 | −50.88729 | 0.55 | 0.36 | 2218 | 1447 | −157 | −57.64 | 6.37 | 252 | 24 | D |
| I16172-5028_1-C1 | 1 | 245.26256 | −50.58708 | 0.72 | 0.43 | 2722 | 1633 | −168 | −53.23 | 5.00 | 165 | 13 | D |
| I16172-5028_1-C1 | 2 | 245.26206 | −50.58693 | 0.77 | 0.36 | 2903 | 1361 | 90 | - | - | - | - | D |
| I16172-5028_1-C1 | 3 | 245.26308 | −50.58686 | 0.48 | 0.14 | 1814 | 544 | 126 | −53.71 | 10.00 | 191 | 17 | D |
| I16172-5028_1-C1 | 4 | 245.26282 | −50.58681 | 0.31 | 0.12 | 1179 | 454 | 46 | −53.71 | 6.78 | 213 | 19 | D |
| I16172-5028_1-C1 | 5 | 245.26247 | −50.58679 | 0.36 | 0.26 | 1361 | 998 | 92 | −52.55 | 5.61 | 254 | 22 | D |
| I16313-4729-C1 | 1 | 248.72672 | −47.59375 | 0.65 | 0.46 | 3234 | 2275 | 153 | - | - | - | - | B* |
| I16348-4654-C2 | 1 | 249.62130 | −47.01219 | 0.36 | 0.29 | 4079 | 3263 | 145 | - | - | - | - | C |
| I16348-4654-C1 | 2 | 249.62350 | −47.01006 | 1.03 | 0.94 | 11,693 | 10,605 | 50 | - | - | - | - | B* |
| I16351-4722-C1 | 1 | 249.71040 | −47.46686 | 1.68 | 1.32 | 3914 | 3076 | 124 | - | - | - | - | B |
| I16445-4459-C1 | 1 | 252.02145 | −45.08560 | 0.67 | 0.48 | 5188 | 3706 | 45 | - | - | - | - | A |
| I16458-4512-C1 | 1 | 252.37523 | −45.29565 | 0.55 | 0.36 | 2313 | 1508 | 67 | −51.44 | 4.00 | 240 | 21 | A* |
| I16562-3959-C1 | 1 | 254.92345 | −40.06211 | 0.19 | 0.12 | 263 | 164 | 78 | −16.95 | 5.96 | 212 | 14 | C* |
| I16562-3959-C1 | 2 | 254.92327 | −40.06196 | 0.43 | 0.24 | 592 | 329 | −144 | −14.56 | 4.32 | 436 | 69 | C |
| I17016-4124-C1 | 1 | 256.29549 | −41.48524 | 1.49 | 0.94 | 4702 | 2958 | 101 | - | - | - | - | A |
| I17016-4124-C3 | 2 | 256.29666 | −41.48537 | 0.74 | 0.36 | 2351 | 1138 | 163 | −27.99 | 4.00 | 302 | 33 | D |
| I17016-4124-C2 | 3 | 256.29625 | −41.48415 | 0.22 | 0.17 | 683 | 531 | 176 | - | - | - | - | A |
| I17143-3700-C1 | 1 | 259.43941 | −37.05362 | 0.50 | 0.38 | 5902 | 4497 | 133 | −32.57 | 4.37 | 258 | 22 | C* |
| I17143-3700-C1 | 2 | 259.43929 | −37.05328 | 0.86 | 0.53 | 10,117 | 6183 | −174 | - | - | - | - | A |
| I17160-3707-C1 | 1 | 259.86426 | −37.18547 | 0.48 | 0.38 | 4934 | 3948 | 153 | −67.98 | 7.28 | 647 | 175 | C |
| I17160-3707-C2 | 2 | 259.86252 | −37.18150 | 0.36 | 0.26 | 3701 | 2714 | −178 | −68.90 | 10.00 | 272 | 27 | A |
| I17175-3544-C3 | 1 | 260.22251 | −35.78431 | 0.91 | 0.50 | 1204 | 665 | 62 | −7.35 | 2.15 | 159 | 9 | D |
| I17175-3544-C2 | 2 | 260.22151 | −35.78307 | 0.79 | 0.74 | 1045 | 982 | 129 | - | - | - | - | C |
| I17175-3544-C1 | 3 | 260.22254 | −35.78292 | 1.18 | 0.58 | 1552 | 760 | 67 | - | - | - | - | B |
| I17175-3544-C2 | 4 | 260.22168 | −35.78278 | 0.48 | 0.31 | 634 | 412 | 121 | - | - | - | - | C |
| I17175-3544-C1 | 5 | 260.22249 | −35.78258 | 0.89 | 0.46 | 1172 | 602 | 105 | - | - | - | - | B |
| I17175-3544-C1 | 6 | 260.22275 | −35.78257 | 0.41 | 0.14 | 539 | 190 | 66 | - | - | - | - | B |
| I17175-3544-C1 | 7 | 260.22252 | −35.78226 | 0.19 | 0.17 | 253 | 222 | 120 | −6.21 | 10.00 | 798 | 255 | B |
| I17204-3636-C1 | 1 | 260.95920 | −36.64989 | 0.50 | 0.31 | 1648 | 1020 | −166 | −17.65 | 9.47 | 234 | 26 | A |
| I17220-3609-C1 | 1 | 261.35518 | −36.21275 | 0.34 | 0.29 | 2705 | 2318 | 119 | - | - | - | - | D |
| I17220-3609-C1 | 2 | 261.35543 | −36.21274 | 0.26 | 0.19 | 2125 | 1546 | 116 | - | - | - | - | A |
| I17220-3609-C1 | 3 | 261.35526 | −36.21232 | 0.91 | 0.50 | 7342 | 4057 | 69 | - | - | - | - | A |
| I17220-3609-C1 | 4 | 261.35564 | −36.21228 | 0.41 | 0.31 | 3284 | 2512 | −178 | - | - | - | - | B |
| I17220-3609-C1 | 5 | 261.35509 | −36.21204 | 0.22 | 0.17 | 1739 | 1352 | −177 | −92.88 | 4.94 | 177 | 12 | C |
| I17271-3439_1-C2 | 1 | 262.61076 | −34.69651 | 0.26 | 0.22 | 966 | 791 | 156 | −13.09 | 8.86 | 198 | 27 | C |
| I17271-3439_1-C1 | 2 | 262.60917 | −34.69607 | 0.41 | 0.24 | 1493 | 878 | −154 | −19.28 | 2.84 | 103 | 6 | D |
| I17545-2357-C1 | 1 | 269.39499 | −23.96824 | 0.55 | 0.29 | 1656 | 864 | 68 | 7.24 | 2.37 | 125 | 10 | D |
| I17599-2148-C1 | 1 | 270.75307 | −21.80283 | 0.65 | 0.48 | 2229 | 1651 | −178 | - | - | - | - | A |

**Table B1**
(Continued)

| Core | Fragment | R.A. (deg) | Decl. (deg) | Maj_FWHM (arcsec) | Min_FWHM (arcsec) | Maj_size (au) | Min_size (au) | PA (deg) | Vlsr (km s$^{-1}$) | Line Width (km s$^{-1}$) | $T_{kin}$ (K) | ERR$_T$ (K) | Flag[a] |
|---|---|---|---|---|---|---|---|---|---|---|---|---|---|
| (1) | (2) | (3) | (4) | (5) | (6) | (7) | (8) | (9) | (10) | (11) | (12) | (13) | (14) |
| I18032-2032-C3 | 1 | 271.56222 | −20.52871 | 0.50 | 0.36 | 2419 | 1728 | 94 | 4.41 | 3.96 | 175 | 11 | D |
| I18032-2032-C2 | 2 | 271.56199 | −20.52762 | 1.10 | 0.62 | 5299 | 2995 | 99 | - | - | - | - | A |
| I18032-2032-C4 | 3 | 271.56169 | −20.52700 | 0.82 | 0.50 | 3917 | 2419 | −153 | - | - | - | - | A |
| I18032-2032-C1 | 4 | 271.56121 | −20.52575 | 0.17 | 0.17 | 806 | 806 | 103 | 3.64 | 6.48 | 189 | 15 | C |
| I18032-2032-C1 | 5 | 271.56114 | −20.52543 | 0.72 | 0.67 | 3456 | 3226 | 88 | - | - | - | - | A |
| I18056-1952-C1 | 1 | 272.15941 | −19.86408 | 0.82 | 0.48 | 6887 | 4051 | 125 | - | - | - | - | D |
| I18056-1952-C1 | 2 | 272.15923 | −19.86397 | 0.70 | 0.43 | 5874 | 3646 | 131 | - | - | - | - | D |
| I18110-1854-C1 | 1 | 273.50369 | −18.89062 | 0.36 | 0.26 | 1141 | 837 | 160 | - | - | - | - | C |
| I18116-1646-C1 | 1 | 273.64941 | −16.76006 | 0.19 | 0.14 | 741 | 556 | 161 | 47.46 | 9.68 | 102 | 16 | C |
| I18116-1646-C1 | 2 | 273.64933 | −16.75996 | 0.24 | 0.22 | 926 | 834 | 77 | 48.46 | 5.67 | 198 | 25 | A |
| I18434-0242-C1 | 1 | 281.51575 | −2.65621 | 1.46 | 0.96 | 6969 | 4570 | −172 | - | - | - | - | A |
| I18469-0132-C1 | 1 | 282.38772 | −1.48432 | 1.03 | 0.74 | 5067 | 3653 | 78 | 87.26 | 10.00 | 722 | 211 | B* |
| I18479-0005-C1 | 1 | 282.62806 | −0.03312 | 0.67 | 0.62 | 8649 | 8031 | 55 | - | - | - | - | C |
| I18507+0110-C1 | 1 | 283.32779 | 1.24862 | 0.46 | 0.43 | 1473 | 1395 | 47 | - | - | - | - | A |
| I18507+0110-C1 | 2 | 283.32793 | 1.24886 | 0.50 | 0.26 | 1628 | 853 | 161 | - | - | - | - | A |
| I18507+0110-C1 | 3 | 283.32817 | 1.24892 | 0.17 | 0.14 | 543 | 465 | −164 | 56.06 | 2.75 | 157 | 7 | C |
| I18507+0110-C1 | 4 | 283.32795 | 1.24935 | 0.24 | 0.19 | 775 | 620 | −173 | - | - | - | - | A |
| I18507+0110-C1 | 5 | 283.32733 | 1.24943 | 0.43 | 0.31 | 1395 | 1008 | 132 | - | - | - | - | D |
| I18507+0110-C1 | 6 | 283.32785 | 1.24947 | 0.36 | 0.29 | 1163 | 930 | 124 | - | - | - | - | C |
| I18507+0110-C1 | 7 | 283.32760 | 1.24954 | 0.58 | 0.17 | 1860 | 543 | 140 | - | - | - | - | D |
| I18507+0110-C1 | 8 | 283.32764 | 1.24981 | 0.17 | 0.14 | 543 | 465 | −164 | 59.76 | 7.59 | 528 | 80 | D |
| I19078+0901-C1 | 1 | 287.55586 | 9.10297 | 0.72 | 0.48 | 8273 | 5515 | 93 | 3.49 | 5.12 | 138 | 9 | A |
| I19078+0901-C3 | 2 | 287.55292 | 9.10314 | 0.53 | 0.46 | 6067 | 5239 | 158 | 12.94 | 8.17 | 222 | 15 | C |
| I19078+0901-C3 | 3 | 287.55361 | 9.10319 | 0.26 | 0.14 | 3033 | 1655 | 117 | 13.78 | 8.26 | 199 | 17 | D |
| I19078+0901-C2 | 4 | 287.55486 | 9.10368 | 1.80 | 1.08 | 20,682 | 12,409 | 107 | 17.54 | 7.90 | 452 | 125 | D |
| I19078+0901-C3 | 5 | 287.55365 | 9.10333 | 0.24 | 0.12 | 2758 | 1379 | 133 | 12.15 | 10.00 | 236 | 25 | D |
| I19078+0901-C1 | 6 | 287.55597 | 9.10351 | 0.74 | 0.60 | 8549 | 6894 | 171 | 2.14 | 7.92 | 307 | 54 | D |
| I19078+0901-C2 | 7 | 287.55534 | 9.10353 | 0.65 | 0.50 | 7446 | 5791 | 178 | 8.56 | 6.02 | 348 | 64 | A |
| I19078+0901-C5 | 8 | 287.55554 | 9.10449 | 0.91 | 0.60 | 10,479 | 6894 | −162 | 3.80 | 5.09 | 161 | 9 | C |
| I19078+0901-C4 | 9 | 287.55472 | 9.10521 | 0.34 | 0.24 | 3861 | 2758 | −176 | 6.89 | 5.11 | 182 | 15 | D |
| I19095+0930-C1 | 1 | 287.97498 | 9.59732 | 0.89 | 0.82 | 8054 | 7401 | 154 | 41.45 | 8.28 | 508 | 116 | C* |
| I19097+0847-C2 | 1 | 288.03759 | 8.87062 | 0.67 | 0.38 | 5262 | 3007 | 53 | 59.34 | 7.98 | 142 | 18 | A |
| I19097+0847-C1 | 2 | 288.03840 | 8.87082 | 0.53 | 0.48 | 4134 | 3758 | 139 | 59.39 | 7.39 | 350 | 41 | A |

**Note.**
[a] "A" denotes HMFs that are associated with jetlike outflow. "B" denotes HMFs that are associated with wide-angle outflow. "C" denotes hot cores without outflow or with weak outflow. "D" denotes shell-like HMFs, which appear more like shells around HC/UC H II regions and lack significant associated 1.3 mm continuum emission. An asterisk denotes that the $CH_3CN$ emission spatially coincides with the H30$\alpha$ emission.

## Appendix C
## HC/UC H II Region Catalog

Using `astrodendro`, the HC/UC H II regions were identified in the H30$\alpha$ emission maps. The `astrodendro` parameters were configured with `min_delta` = 3$\sigma$ and `min_value` = 5$\sigma$. Table C1, columns (3)–(8), are H30$\alpha$ line integrated intensity peak coordinates R.A. and decl., intensity-weighted second moments along the major and minor axes, position angle measured from north to east, and size ($=\sqrt{\text{Mag\_FWHM} \times \text{Min\_FWHM}}$). Additionally, Gaussian fittings were performed to derive the physical parameters including central velocity (column (9)), line width (column (10)), and amplitude (column (11)) from the averaged H30$\alpha$ spectra of these identified HC/UC H II region. Figure C1 presents the relation between their size and line width.

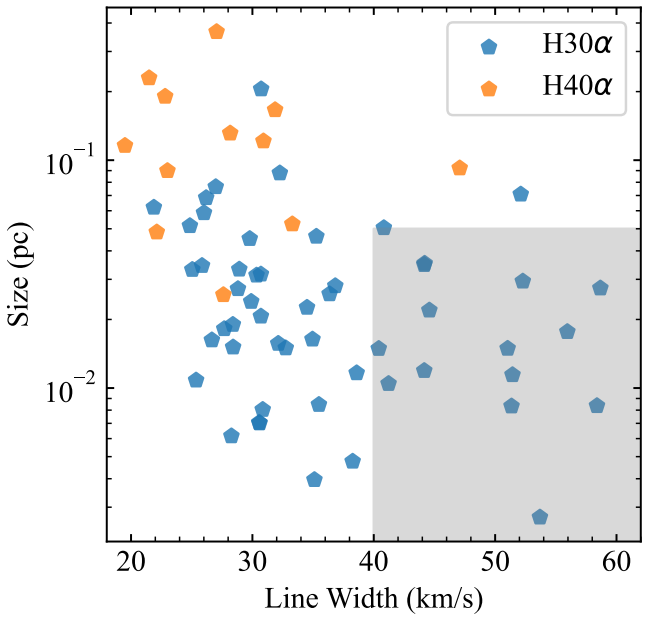


**Figure C1.** Relation between the size and the line width of the ionized gas structure. The sizes and line widths of these ionized gas structures were measured from H30$\alpha$ (blue pentagons) or H40$\alpha$ (orange pentagons). Those located in the gray shaded region are regarded as candidate HC H II regions, while the rest are regarded as candidate UC H II regions.

**Table C1**
Physical Parameters of the HC/UC H II Regions

| Field | ID | R.A. (deg) | Decl. (deg) | Maj_FWHM (arcsec) | Min_FWHM (arcsec) | PA (deg) | Size (au) | Vlsr (km s$^{-1}$) | Line Width (km s$^{-1}$) | Amplitude (Jy beam$^{-1}$) | Type |
|---|---|---|---|---|---|---|---|---|---|---|---|
| (1) | (2) | (3) | (4) | (5) | (6) | (7) | (8) | (9) | (10) | (11) | (12) |
| I12320-6122 | 1 | 188.72186 | −61.66111 | 0.58 | 0.55 | 102 | 2402 | −39.25 | 38.59 | 0.1611 | UC |
| I12326-6245 | 1 | 188.89618 | −63.04219 | 0.43 | 0.36 | −149 | 1718 | −70.70 | 51.35 | 2.0680 | HC |
| I12572-6316_1 | 1 | 195.10028 | −63.54215 | 0.34 | 0.26 | 106 | 3349 | 24.60 | 26.66 | 0.0348 | UC |
| I13471-6120 | 1 | 207.67410 | −61.58617 | 1.10 | 0.96 | 77 | 5335 | −57.62 | 36.36 | 0.2147 | UC |
| I15254-5621 | 1 | 232.33076 | −56.52285 | 0.72 | 0.70 | 137 | 3076 | −69.48 | 51.03 | 0.4050 | HC |
| I15290-5546 | 1 | 233.22192 | −55.93608 | 3.31 | 1.58 | 175 | 18,103 | −88.52 | 32.26 | 0.0605 | UC |
| I15290-5546 | 2 | 233.22174 | −55.93468 | 1.97 | 1.58 | 172 | 14,101 | −89.90 | 26.19 | 0.0610 | UC |
| I15411-5352 | 1 | 236.24718 | −54.03887 | 4.73 | 1.68 | −169 | 6825 | −44.91 | 25.05 | 0.0325 | UC |
| I15439-5449 | 1 | 236.95870 | −54.97589 | 2.26 | 1.56 | 120 | 6446 | −53.21 | 30.34 | 0.0157 | UC |
| I15502-5302 | 1 | 238.52668 | −53.19468 | 2.23 | 1.61 | −146 | 10,409 | −93.86 | 40.83 | 0.2007 | UC |
| I15520-5234 | 1 | 238.95153 | −52.71856 | 2.02 | 0.72 | −166 | 3072 | −41.96 | 40.41 | 0.0860 | HC |
| I15520-5234 | 2 | 238.95222 | −52.71853 | 0.43 | 0.36 | 137 | 983 | −40.89 | 38.26 | 0.2972 | UC |
| I15520-5234 | 3 | 238.95273 | −52.71836 | 0.72 | 0.55 | 149 | 1659 | −35.95 | 30.85 | 0.1597 | UC |
| I15567-5236 | 1 | 240.13813 | −52.74651 | 2.62 | 0.60 | 172 | 6515 | −107.51 | 30.70 | 0.0472 | UC |
| I15567-5236 | 2 | 240.13701 | −52.74624 | 1.51 | 0.43 | 66 | 4260 | −112.36 | 30.70 | 0.0492 | UC |
| I15567-5236 | 3 | 240.13788 | −52.74604 | 2.18 | 0.89 | −137 | 7266 | −113.18 | 44.19 | 0.0734 | HC |
| I16037-5223 | 1 | 241.90610 | −52.51699 | 1.63 | 1.22 | 165 | 12,801 | −80.06 | 21.88 | 0.0495 | UC |
| I16037-5223 | 2 | 241.91185 | −52.51662 | 1.10 | 0.98 | −150 | 9329 | −78.59 | 29.78 | 0.0335 | UC |
| I16037-5223 | 3 | 241.90884 | −52.51493 | 1.15 | 0.98 | −176 | 9546 | −78.77 | 35.27 | 0.1029 | UC |
| I16060-5146 | 1 | 242.46825 | −51.91604 | 0.82 | 0.58 | 124 | 3751 | −86.72 | 27.68 | 0.1173 | UC |
| I16060-5146 | 2 | 242.46944 | −51.91539 | 0.65 | 0.55 | 116 | 3234 | −92.48 | 32.13 | 0.8439 | UC |
| I16060-5146 | 3 | 242.46843 | −51.91499 | 0.94 | 0.72 | 61 | 4528 | −83.13 | 44.58 | 0.2740 | HC |
| I16060-5146 | 4 | 242.46947 | −51.91501 | 0.48 | 0.41 | 103 | 2458 | −89.82 | 44.16 | 1.7127 | HC |
| I16065-5158 | 1 | 242.58458 | −52.10186 | 9.62 | 6.53 | 97 | 34,294 | - | - | - | UC |

**Table C1**
(Continued)

| Field | ID | R.A. (deg) | Decl. (deg) | Maj_FWHM (arcsec) | Min_FWHM (arcsec) | PA (deg) | Size (au) | Vlsr (km s$^{-1}$) | Line Width (km s$^{-1}$) | Amplitude (Jy beam$^{-1}$) | Type |
|---|---|---|---|---|---|---|---|---|---|---|---|
| (1) | (2) | (3) | (4) | (5) | (6) | (7) | (8) | (9) | (10) | (11) | (12) |
| I16071-5142 | 1 | 242.74752 | −51.83989 | 3.53 | 3.50 | −142 | 18,536 | - | - | - | UC |
| I16164-5046 | 1 | 245.04616 | −50.88731 | 0.84 | 0.82 | −168 | 3377 | −64.26 | 34.95 | 0.5454 | UC |
| I16164-5046 | 2 | 245.04541 | −50.88729 | 0.41 | 0.34 | 178 | 1447 | −56.29 | 30.59 | 0.2154 | UC |
| I16172-5028_1 | 1 | 245.26199 | −50.58711 | 0.24 | 0.19 | −141 | 816 | −50.54 | 35.11 | 0.1552 | UC |
| I16172-5028_1 | 2 | 245.26227 | −50.58686 | 0.48 | 0.43 | 112 | 1724 | −65.45 | 58.39 | 0.9693 | HC |
| I16172-5028_1 | 3 | 245.26265 | −50.58671 | 0.48 | 0.24 | 105 | 1270 | −49.75 | 28.27 | 0.3915 | UC |
| I16313-4729 | 1 | 248.72676 | −47.59372 | 0.46 | 0.41 | 140 | 2156 | −75.86 | 41.22 | 0.0880 | HC |
| I16348-4654 | 1 | 249.62350 | −47.00986 | 2.30 | 2.11 | −176 | 25,017 | - | - | - | UC |
| I16351-4722 | 1 | 249.71030 | −47.46750 | 0.72 | 0.55 | 178 | 1454 | −32.97 | 30.56 | 0.0544 | UC |
| I16445-4459 | 1 | 252.02158 | −45.08617 | 3.26 | 2.90 | 143 | 23,901 | - | - | - | UC |
| I16458-4512 | 1 | 252.37521 | −45.29569 | 0.84 | 0.67 | −154 | 3117 | −53.05 | 28.41 | 0.0575 | UC |
| I16562-3959 | 1 | 254.92345 | −40.06212 | 0.43 | 0.41 | 132 | 559 | −12.35 | 53.69 | 0.1069 | HC |
| I17016-4124 | 1 | 256.29668 | −41.48531 | 0.58 | 0.53 | 119 | 1744 | −32.31 | 35.48 | 0.1706 | UC |
| I17143-3700 | 1 | 259.43941 | −37.05362 | 0.55 | 0.41 | 161 | 5621 | −34.22 | 28.81 | 0.0952 | UC |
| I17160-3707 | 1 | 259.86464 | −37.18394 | 7.94 | 6.79 | 125 | 75,496 | - | - | - | UC |
| I17175-3544 | 1 | 260.22276 | −35.78394 | 4.42 | 3.62 | −169 | 5291 | - | - | - | UC |
| I17204-3636 | 1 | 260.95967 | −36.64992 | 3.14 | 2.93 | −157 | 9967 | - | - | - | UC |
| I17220-3609 | 1 | 261.35514 | −36.21268 | 1.42 | 1.25 | 156 | 10,626 | −94.13 | 24.85 | 0.1792 | UC |
| I17271-3439_1 | 1 | 262.60909 | −34.69599 | 1.68 | 0.96 | 165 | 4656 | −12.53 | 34.50 | 0.0460 | UC |
| I17545-2357 | 1 | 269.39508 | −23.96822 | 0.79 | 0.70 | 171 | 2232 | 7.80 | 25.36 | 0.0474 | UC |
| I17599-2148 | 1 | 270.75571 | −21.80328 | 10.94 | 5.64 | 135 | 27,080 | - | - | - | UC |
| I17599-2148 | 2 | 270.75320 | −21.80239 | 3.38 | 2.93 | 57 | 10,815 | - | - | - | UC |
| I18032-2032 | 1 | 271.56224 | −20.52864 | 0.91 | 0.72 | 138 | 3917 | 10.67 | 28.39 | 0.0481 | UC |
| I18056-1952 | 1 | 272.15920 | −19.86394 | 2.45 | 2.06 | −171 | 19,041 | - | - | - | UC |
| I18110-1854 | 1 | 273.50417 | −18.89025 | 2.81 | 1.66 | 142 | 6847 | 41.31 | 28.92 | 0.0215 | UC |
| I18116-1646 | 1 | 273.64796 | −16.76078 | 16.44 | 9.14 | −162 | 47,339 | - | - | - | UC |
| I18434-0242 | 1 | 281.51637 | −2.65608 | 3.98 | 1.61 | 62 | 12,109 | 100.62 | 26.01 | 0.0472 | UC |
| I18469-0132 | 1 | 282.38772 | −1.48431 | 0.55 | 0.46 | 162 | 2357 | 96.12 | 51.43 | 0.0722 | HC |
| I18479-0005 | 1 | 282.62771 | −0.03361 | 0.62 | 0.48 | 166 | 7104 | 16.37 | 25.85 | 0.1962 | UC |
| I18479-0005 | 2 | 282.62793 | −0.03349 | 0.26 | 0.22 | 127 | 3089 | 12.60 | 32.75 | 0.1048 | UC |
| I18479-0005 | 3 | 282.62783 | −0.03328 | 0.46 | 0.34 | 134 | 4942 | 2.52 | 29.90 | 0.0966 | UC |
| I18479-0005 | 4 | 282.62797 | −0.03283 | 1.44 | 1.03 | −171 | 15,753 | 12.18 | 26.98 | 0.0331 | UC |
| I18479-0005 | 5 | 282.62912 | −0.03243 | 5.30 | 2.04 | 51 | 42,317 | 19.33 | 30.72 | 0.0179 | UC |
| I18507+0110 | 1 | 283.32742 | 1.24949 | 1.25 | 1.01 | 88 | 3643 | 50.51 | 55.95 | 1.0739 | HC |
| I19078+0901 | 1 | 287.55592 | 9.10361 | 2.14 | 0.74 | −151 | 14,615 | 14.16 | 52.11 | 0.5309 | UC |
| I19078+0901 | 2 | 287.55371 | 9.10325 | 0.55 | 0.50 | 99 | 6067 | 14.71 | 52.28 | 0.4158 | HC |
| I19078+0901 | 3 | 287.55479 | 9.10353 | 0.74 | 0.50 | 137 | 7170 | 15.66 | 44.16 | 0.8211 | HC |
| I19078+0901 | 4 | 287.55478 | 9.10521 | 0.50 | 0.48 | −173 | 5791 | −3.09 | 36.83 | 0.3094 | UC |
| I19095+0930 | 1 | 287.97498 | 9.59728 | 0.67 | 0.60 | 171 | 5660 | 66.82 | 58.67 | 0.1135 | HC |
| I19097+0847 | 1 | 288.03641 | 8.86911 | 5.71 | 4.37 | 131 | 39,275 | - | - | - | UC |

**Note.** A hyphen indicates that H30$\alpha$ is not detected in ALMA band 6. Therefore, we use H40$\alpha$ (ALMA Band 3) line integrated intensity for HC/UC H II region identification.

## Appendix D
## Images for All Selected Fields

In this section, we present the complete set of images for our sample. Each field is displayed in a two-panel format with the following configuration: left panel, the ATOMS Band 3 3.0 mm continuum (gray contours) and H40$\alpha$ line integrated intensity (green color); right panel, the QUARKS Band 6 1.3 mm continuum (gray contours) and H30$\alpha$ line integrated intensity (green color). Additionally, the QUARKS $^{12}$CO (2–1) outflow (red and blue colors) and $CH_3CN$ ($12_3$–$11_3$) line integrated intensity (orange contours) are overlaid on both panels. The details can be found in the caption of Figure D1.

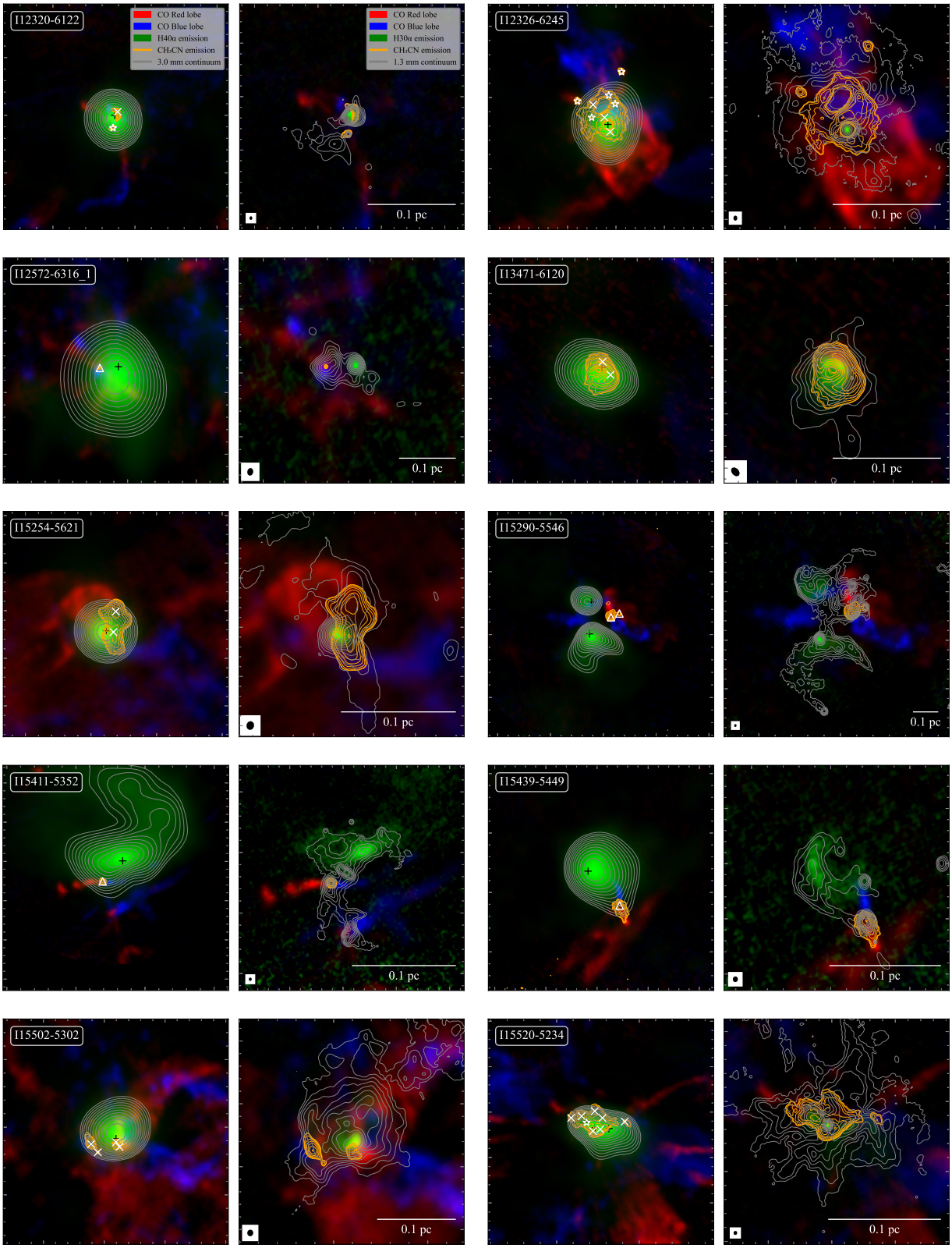


**Figure D1.** Images of the hydrogen recombination line emission and the outflow for our sample. In the left panels for each source, the background shows the three-color image composed by the $^{12}$CO (2–1) outflow red lobe (red), H40$\alpha$ (green) and $^{12}$CO (2–1) outflow blue lobe (blue), and the gray contours and orange contours represent the 3 mm continuum and the $CH_3CN$ ($12_3$–$11_3$) integrated line emission, respectively. In the right panels for each source, the green background and gray contours represent H30$\alpha$ and 1.3 mm continuum, and the others are the same as the panel on the left. The H30$\alpha$/H40$\alpha$ integrated velocity range is [Vlsr–40 km s$^{-1}$, Vlsr+40 km s$^{-1}$], where Vlsr is the central velocity. For $CH_3CN$ ($12_3$–$11_3$), the integrated velocity ranges are different for different fields. Similarly, distinct integrated velocity ranges were adopted for $^{12}$CO (2–1) to avoid contamination and clearly reveal the outflow features. The contour levels were plotted from 3$\sigma$ to the peak intensity of the field, with eight logarithmically spaced contours between these values. White markers mark the positions of the HMFs (jetlike outflow, triangles; wide-angle outflow, pentagons; no/weak outflow, stars; shell-like, crosses), while black plus signs indicate the locations of the HC/UC H II regions. The synthesized beams are shown in the lower left corner of the right panel, while the scale bar is indicated in the lower right corner.

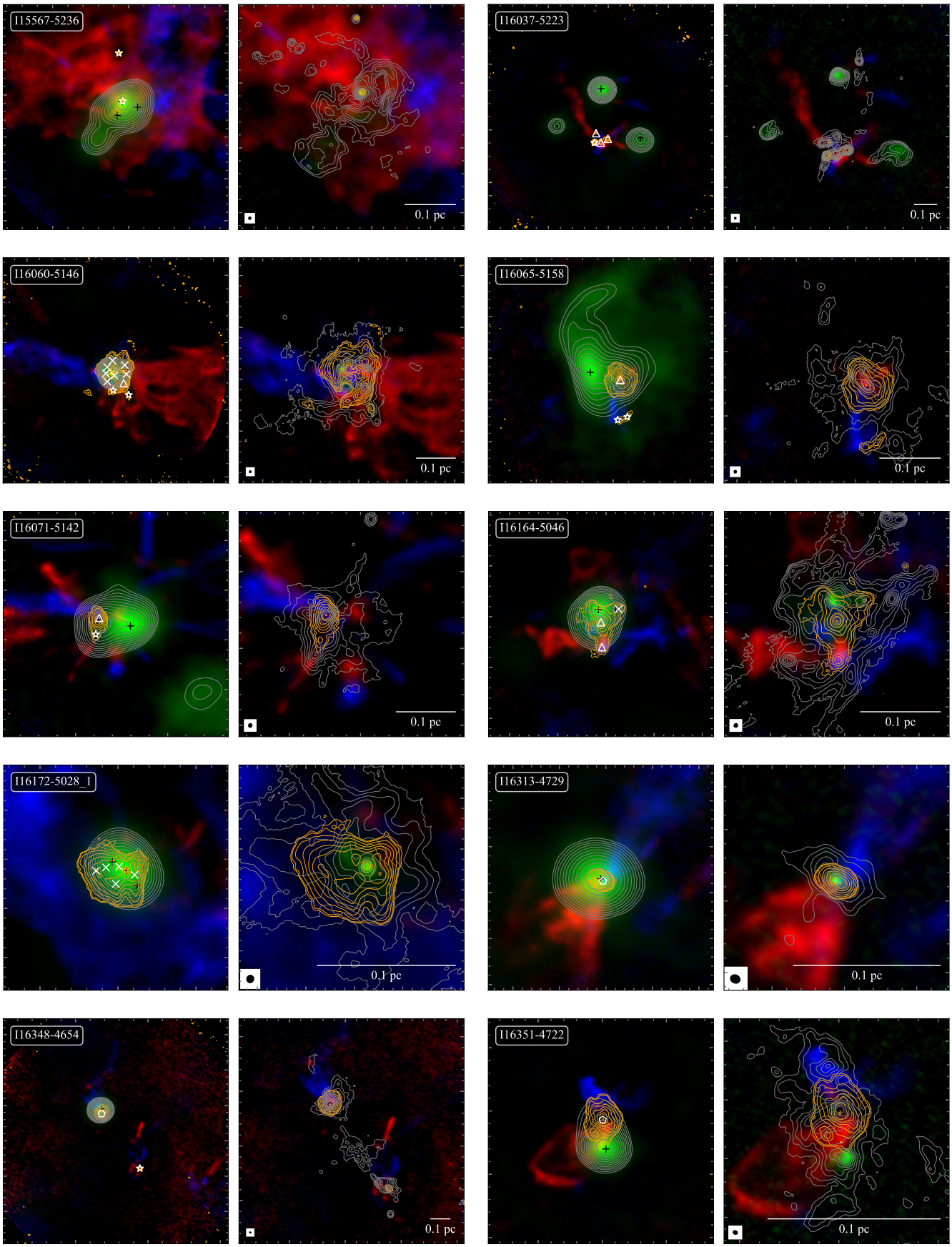


**Figure D1.** (Continued.)

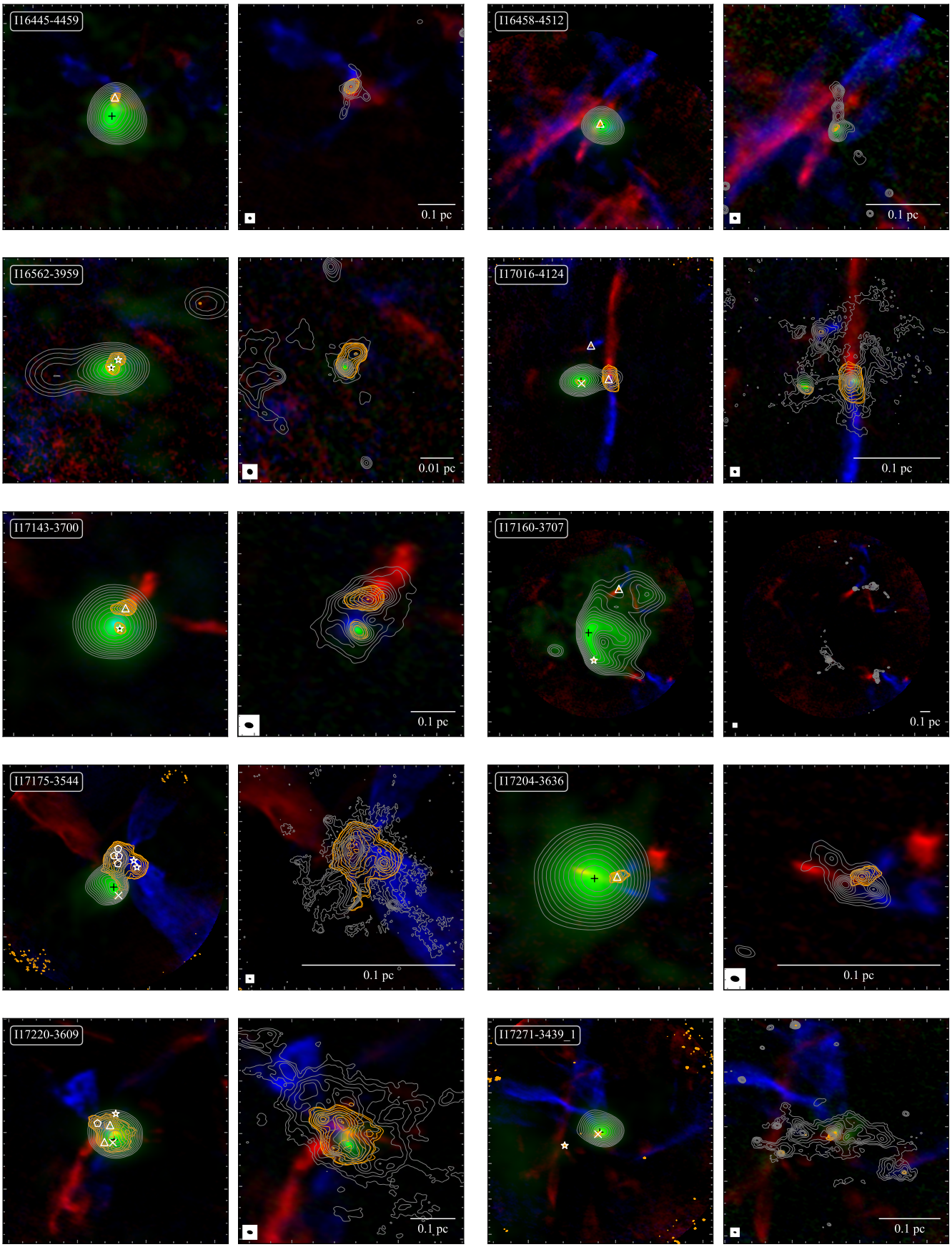


**Figure D1.** (Continued.)

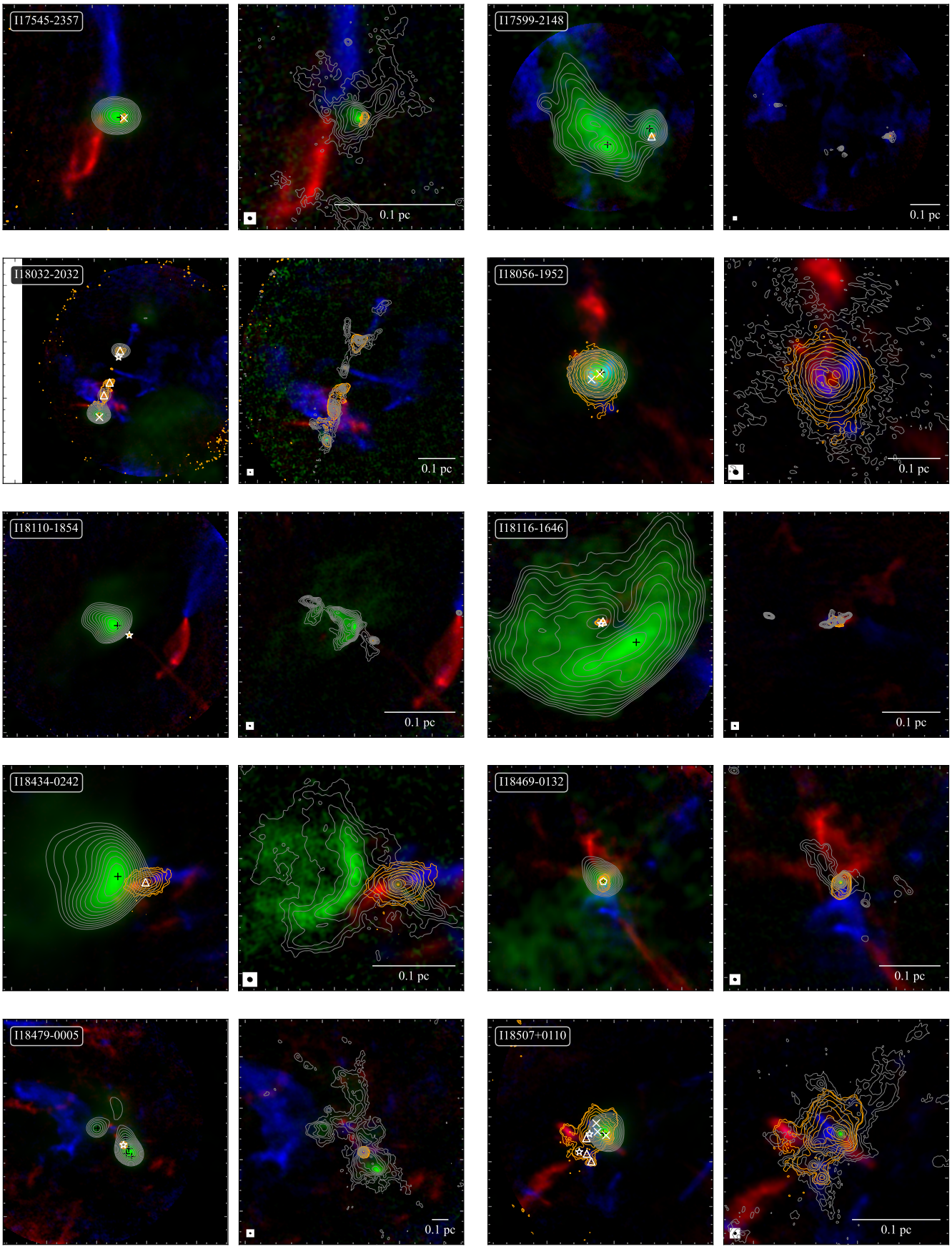


**Figure D1.** (Continued.)

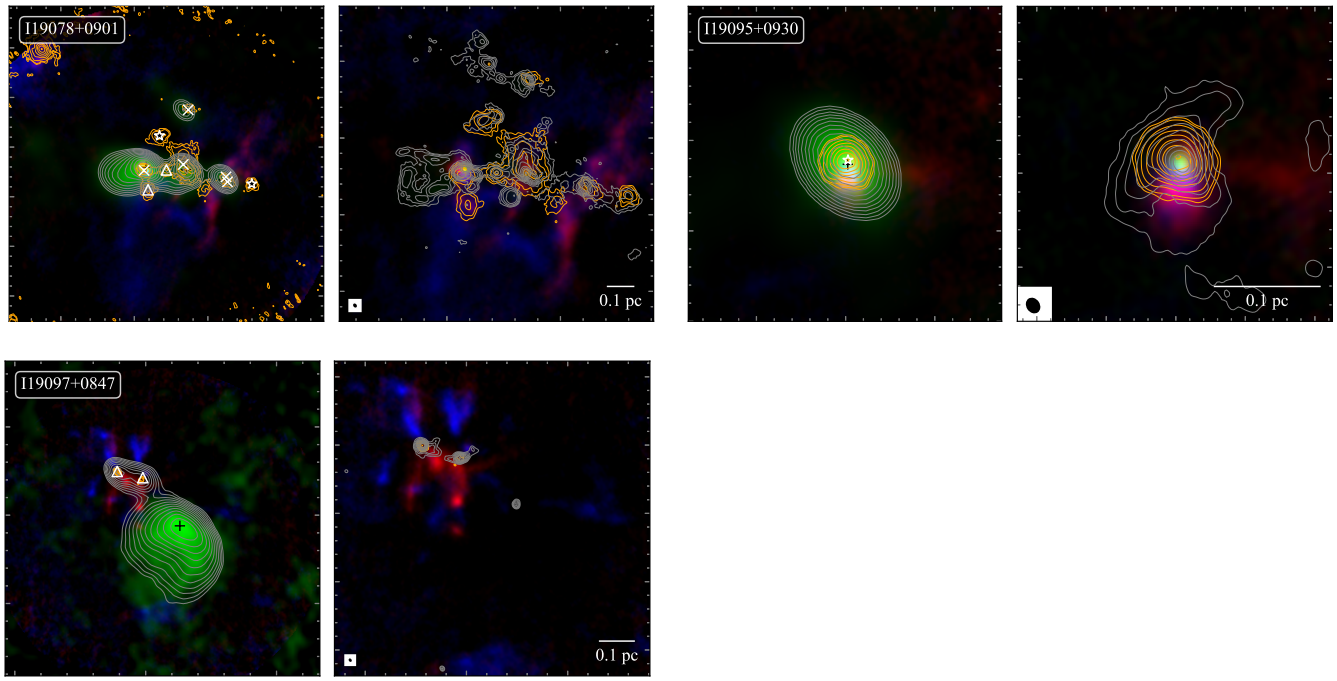


**Figure D1.** (Continued.)

## ORCID iDs

Dezhao Meng https://orcid.org/0009-0000-5764-8527
Tie Liu https://orcid.org/0000-0002-5286-2564
Jarken Esimbek https://orcid.org/0000-0003-4910-1390
Sheng-Li Qin https://orcid.org/0000-0003-2302-0613
Guido Garay https://orcid.org/0000-0003-1649-7958
Paul F. Goldsmith https://orcid.org/0000-0002-6622-8396
Jianjun Zhou https://orcid.org/0000-0003-0356-818X
Xindi Tang https://orcid.org/0000-0002-4154-4309
Wenyu Jiao https://orcid.org/0000-0001-9822-7817
Yan-Kun Zhang https://orcid.org/0000-0001-7817-1975
Fengwei Xu https://orcid.org/0000-0001-5950-1932
Siju Zhang https://orcid.org/0000-0002-9836-0279
Anandmayee Tej https://orcid.org/0000-0001-5917-5751
Leonardo Bronfman https://orcid.org/0000-0002-9574-8454
Aiyuan Yang https://orcid.org/0000-0003-4546-2623
Sami Dib https://orcid.org/0000-0002-8697-9808
Swagat R. Das https://orcid.org/0000-0002-3658-0516
Jihye Hwang https://orcid.org/0000-0001-7866-2686
Archana Soam https://orcid.org/0000-0002-6386-2906
Yisheng Qiu https://orcid.org/0000-0002-7716-1094
Dalei Li https://orcid.org/0000-0001-5494-6238
Yuxin He https://orcid.org/0000-0002-8760-8988
Gang Wu https://orcid.org/0000-0003-0933-7112
Lokesh Dewangan https://orcid.org/0000-0001-6725-0483
James O. Chibueze https://orcid.org/0000-0002-9875-7436
Pablo García https://orcid.org/0000-0002-8586-6721
Prasanta Gorai https://orcid.org/0000-0003-1602-6849
Naval Kishor Bhadari https://orcid.org/0000-0001-8812-8460
Yong Zhang https://orcid.org/0000-0002-1086-7922
Patricio Sanhueza https://orcid.org/0000-0002-7125-7685
Yongquan Luo https://orcid.org/0009-0000-8349-7355
Jia-Hang Zou https://orcid.org/0009-0000-9090-9960
Kee-Tae Kim https://orcid.org/0000-0003-2412-7092
Dongting Yang https://orcid.org/0009-0004-6159-5375
Xunchuan Liu https://orcid.org/0000-0001-8315-4248

## References

Arce, H. G., Shepherd, D., Gueth, F., et al. 2007, in Protostars and Planets V, ed. B. Reipurth, D. Jewitt, & K. Keil (Univ. Arizona Press), 245
Astropy Collaboration, Price-Whelan, A. M., Lim, P. L., et al. 2022, ApJ, 935, 167
Belloche, A., Müller, H. S. P., Menten, K. M., Schilke, P., & Comito, C. 2013, A&A, 559, A47
Beltrán, M. T., Cesaroni, R., Rivilla, V. M., et al. 2018, A&A, 615, A141
Berdikhan, D., Esimbek, J., Henkel, C., et al. 2025, A&A, 699, A137
Beuther, H., Churchwell, E. B., McKee, C. F., & Tan, J. C. 2007, in Protostars and Planets V, ed. B. Reipurth, D. Jewitt, & K. Keil (Univ. Arizona Press), 165
Beuther, H., Kuiper, R., & Tafalla, M. 2025, ARA&A, 63, 1
Beuther, H., Zhang, Q., Bergin, E. A., & Sridharan, T. K. 2009, AJ, 137, 406
Bisschop, S. E., Fuchs, G. W., van Dishoeck, E. F., & Linnartz, H. 2007, A&A, 474, 1061
Bøgelund, E. G., Barr, A. G., Taquet, V., et al. 2019, A&A, 628, A2
Bonfand, M., Csengeri, T., Bontemps, S., et al. 2024, A&A, 687, A163
Brand, J., Massi, F., Zavagno, A., Deharveng, L., & Lefloch, B. 2011, A&A, 527, A62
CASA Team, Bean, B., Bhatnagar, S., et al. 2022, PASP, 134, 114501
Cesaroni, R. 2005, IAUS, 227, 59
Choudhury, R., Schilke, P., Stéphan, G., et al. 2015, A&A, 575, A68
Comrie, A., Wang, K.-S., Hsu, S.-C., et al., 2021 CARTA: Cube Analysis and Rendering Tool for Astronomy, Astrophysics Source Code Library, ascl:2103.031
Crockett, N. R., Bergin, E. A., Neill, J. L., et al. 2014, ApJ, 787, 112
Deharveng, L., Lefloc, B., Kurtz, S., et al. 2008, A&A, 482, 585
Deharveng, L., Lefloch, B., Zavagno, A., et al. 2003, A&A, 408, L25
Deharveng, L., Zavagno, A., & Caplan, J. 2005, A&A, 433, 565
Elmegreen, B. G., & Lada, C. J. 1977, ApJ, 214, 725
Fontani, F., Pascucci, I., Caselli, P., et al. 2007, A&A, 470, 639
Fuente, A., Treviño-Morales, S. P., Alonso-Albi, T., et al. 2021, MNRAS, 507, 1886
Garay, G., & Lizano, S. 1999, PASP, 111, 1049
Gerner, T., Beuther, H., Semenov, D., et al. 2014, A&A, 563, A97
Gerner, T., Shirley, Y. L., Beuther, H., et al. 2015, A&A, 579, A80

Gibb, E., Nummelin, A., Irvine, W. M., Whittet, D. C. B., & Bergman, P. 2000, ApJ, 545, 309
Gieser, C., Beuther, H., Semenov, D., et al. 2021, A&A, 648, A66
Gieser, C., Beuther, H., Semenov, D., et al. 2023, A&A, 674, A160
Halfen, D. T., Ilyushin, V. V., & Ziurys, L. M. 2013, ApJ, 767, 66
Hatchell, J., Thompson, M. A., Millar, T. J., & MacDonald, G. H. 1998, A&AS, 133, 29
Jimenez-Serra, I., Codella, C., & Belloche, A. 2025, arXiv:2503.17104
Jørgensen, J. K., Belloche, A., & Garrod, R. T. 2020, ARA&A, 58, 727
Kurtz, S., Cesaroni, R., Churchwell, E., Hofner, P., & Walmsley, C. M. 2000, in Protostars and Planets IV, ed. V. Mannings, A. P. Boss, & S. S. Russell (Univ. Arizona Press), 299
Law, C. J., Zhang, Q., Öberg, K. I., et al. 2021, ApJ, 909, 214
Li, Z.-Y., Liu, X., Liu, T., et al. 2025, A&A, 697, A190
Liu, H.-L., Li, J.-Z., Wu, Y., et al. 2016, ApJ, 818, 95
Liu, H.-L., Liu, T., Evans, N. J., II, et al. 2021, MNRAS, 505, 2801
Liu, H.-L., Wu, Y., Li, J., et al. 2015, ApJ, 798, 30
Liu, S.-Y., Girart, J. M., Remijan, A., & Snyder, L. E. 2002, ApJ, 576, 255
Liu, S.-Y., Mehringer, D. M., & Snyder, L. E. 2001, ApJ, 552, 654
Liu, T., Evans, N. J., Kim, K.-T., et al. 2020, MNRAS, 496, 2790
Liu, T., Lacy, J., Li, P. S., et al. 2017, ApJ, 849, 25
Liu, T., Wu, Y., Zhang, H., & Qin, S.-L. 2012, ApJ, 751, 68
Liu, X., Liu, T., Zhu, L., et al. 2024, RAA, 24, 025009
Meng, D., Esimbek, J., Henkel, C., et al. 2025, A&A, 701, A155
Miyawaki, R., Tsuboi, M., Uehara, K., & Miyazaki, A. 2021, PASJ, 73, 943
Möller, T., Schilke, P., Schmiedeke, A., et al. 2021, A&A, 651, A9
Motte, F., Bontemps, S., & Louvet, F. 2018, ARA&A, 56, 41
Mottram, J. C., Beuther, H., Ahmadi, A., et al. 2020, A&A, 636, A118
Neill, J. L., Bergin, E. A., Lis, D. C., et al. 2014, ApJ, 789, 8
Nickerson, S., Rangwala, N., Colgan, S. W. J., et al. 2021, ApJ, 907, 51
Osorio, M., Susana, L., & Paola, D. 1999, ApJ, 525, 808
Petriella, A., Paron, S., & Giacani, E. 2010, A&A, 513, A44
Pomarès, M., Zavagno, A., Deharveng, L., et al. 2009, A&A, 494, 987
Purcell, C. R. 2006, PhD thesis, Univ. New South Wales
Purcell, C. R., Longmore, S. N., Burton, M. G., et al. 2009, MNRAS, 394, 323
Qin, S.-L., Huang, M., Wu, Y., Xue, R., & Chen, S. 2008, ApJL, 686, L21
Qin, S.-L., Liu, T., Liu, X., et al. 2022, MNRAS, 511, 3463
Qin, S.-L., Schilke, P., Wu, J., et al. 2015, ApJ, 803, 39
Qin, S.-L., Wu, Y., Huang, M., et al. 2010, ApJ, 711, 399
Qiu, Y., Zhang, T., Möller, T., et al. 2025, ApJS, 277, 21
Rosero, V., Hofner, P., Kurtz, S., Bieging, J., & Araya, E. D. 2013, ApJS, 207, 12
Rosolowsky, E. W., Pineda, J. E., Kauffmann, J., & Goodman, A. A. 2008, ApJ, 679, 1338
Sakai, T., Shiomura, N., Sanhueza, P., et al. 2025, ApJ, 983, 37
Schilke, P., Benford, D. J., Hunter, T. R., Lis, D. C., & Phillips, T. G. 2001, ApJS, 132, 281
Schilke, P., Comito, C., Thorwirth, S., et al. 2006, A&A, 454, L41
Schilke, P., Groesbeck, T. D., Blake, G. A., & Phillips, T. G. 1997, ApJS, 108, 301
Tan, J. C., Beltrán, M. T., Caselli, P., et al. 2014, in Protostars and Planets VI, ed. H. Beuther et al. (Univ. Arizona Press), 149
Taniguchi, K., Sanhueza, P., Olguin, F. A., et al. 2023, ApJ, 950, 57
van der Tak, F. F. S., Black, J. H., Schöier, F. L., Jansen, D. J., & van Dishoeck, E. F. 2007, A&A, 468, 627
van der Tak, F. F. S., van Dishoeck, E. F., & Caselli, P. 2000, A&A, 361, 327
van der Walt, S. J., Kristensen, L. E., Jørgensen, J. K., et al. 2021, A&A, 655, A86
Whitworth, A. P., Bhattal, A. S., Chapman, S. J., Disney, M. J., & Turner, J. A. 1994, MNRAS, 268, 291
Williams, G. M., Cyganowski, C. J., Brogan, C. L., et al. 2022, MNRAS, 509, 748
Wu, Y., Liu, T., & Qin, S.-L. 2014, ApJ, 791, 123
Xu, F., Wang, K., Liu, T., et al. 2024a, ApJS, 270, 9
Xu, F., Wang, K., Liu, T., et al. 2024b, RAA, 24, 065011
Xu, F.-W., Wang, K., Liu, T., et al. 2023, MNRAS, 520, 3259
Yang, A. Y., Thompson, M. A., Tian, W. W., et al. 2019, MNRAS, 482, 2681
Yang, A. Y., Urquhart, J. S., Thompson, M. A., et al. 2021, A&A, 645, A110
Yang, D., Liu, H.-L., Liu, T., et al. 2025, ApJS, 280, 33
Zapata, L. A., Schmid-Burgk, J., & Menten, K. M. 2011, A&A, 529, A24
Zavagno, A., Deharveng, L., Comerón, F., et al. 2006, A&A, 446, 171
Zavagno, A., Pomarès, M., Deharveng, L., et al. 2007, A&A, 472, 835
Zhou, J., Zhou, D., Esimbek, J., et al. 2020, ApJ, 897, 74
Zinnecker, H., & Yorke, H. W. 2007, ARA&A, 45, 481